Focused RBCC Experiments

Two-Rocket Configuration Experiments and Hydrocarbon/Oxygen Rocket Ejector Experiments

Addendum Report
for
NASA Contract Grant NAG8-1844

Robert J. Santoro and Sibtosh Pal

Propulsion Engineering Research Center
and
Department of Mechanical and Nuclear Engineering
The Pennsylvania State University
University Park, Pennsylvania

September, 2003

PENNSTATE

TABLE OF CONTENTS

ABSTRACT

This addendum report documents the results of two additional efforts for the Rocket Based Combined Cycle (RBCC) rocket-ejector mode research work carried out at the Penn State Propulsion Engineering Research Center in support of NASA's technology development efforts for enabling 3rd generation Reusable Launch Vehicles (RLV). The tasks reported here build on an earlier NASA MSFC funded research program on rocket ejector investigations. The first task investigated the improvements of a gaseous hydrogen/oxygen twin thruster RBCC rocket ejector system over a single rocket system. The second task investigated the performance of a hydrocarbon (liquid JP-7)/gaseous oxygen single thruster rocket-ejector system. To gain a systematic understanding of the rocket-ejector's internal fluid mechanic/combustion phenomena, experiments were conducted with both direct-connect and sea-level static diffusion and afterburning (DAB) configurations for a range of rocket operating conditions. For all experimental conditions, overall system performance was obtained through global measurements of wall static pressure profiles, heat flux profiles and engine thrust. Detailed mixing and combustion information was obtained through Raman spectroscopy measurements of major species (gaseous oxygen, hydrogen, nitrogen and water vapor) for the gaseous hydrogen/oxygen rocket ejector experiments.

1. INTRODUCTION

Recent interest in low cost, reliable access to space has generated increased interest in advanced technology approaches to space transportation systems. A key to the success of such programs lies in the development of advanced propulsion systems capable of achieving the performance and operations goals required for the next generation of space vehicles. One extremely promising approach involves the combination of rocket and air-breathing engines into a rocket-based combined-cycle engine (RBCC). Although there are several design variations for the RBCC engine, the gamut of concepts includes four flight regimes, viz. rocket-ejector, ramjet, scramjet and all-rocket [1]. Of these four flight regimes, the rocket-ejector mode that encompasses the zero to roughly two Mach number range of the flight vehicle, is the least well understood. Studies of RBCC engine concepts are not new and studies dating back thirty years are well documented in the literature. However, studies focused on the rocket-ejector mode of the RBCC cycle are lacking.

The tasks reported in this addendum report builds on an earlier integrated experimental and computational fluid dynamics (CFD) program funded by NASA MSFC to examine critical rocket ejector performance issues. The final report for this program, "Experimental and Analytical Modeling of the Rocket Ejector Mode of a Combined Cycle Rocket-Based Engine" (Original NASA Contract Grant NAS8-40890) was submitted in June 2001 [2]. The objective of this original research program was to obtain new data using advanced optical diagnostics such as Raman spectroscopy and CFD techniques to investigate mixing in the rocket ejector mode. A new research facility for the study of the rocket ejector mode was designed and fabricated for this purpose. The present investigation utilizes the rocket-ejector infrastructure developed for this original program to obtain additional experimental measurements for CFD code validation.

The experimental configuration studied here (and in the original program) is based on the well-known 1968 experimental rocket-ejector study of Odegaard and Stroup [3]. Early on in the program, it was recognized that advancements of both proprietary and classified natures have been made in the last thirty years, however, this particular geometry was chosen as the baseline configuration because it represents the most comprehensive set of data available in the open literature. The scope of the current study was not to simply duplicate the experiments of Odegaard and Stroup, but to build on this study by bringing to bear advances made in diagnostic

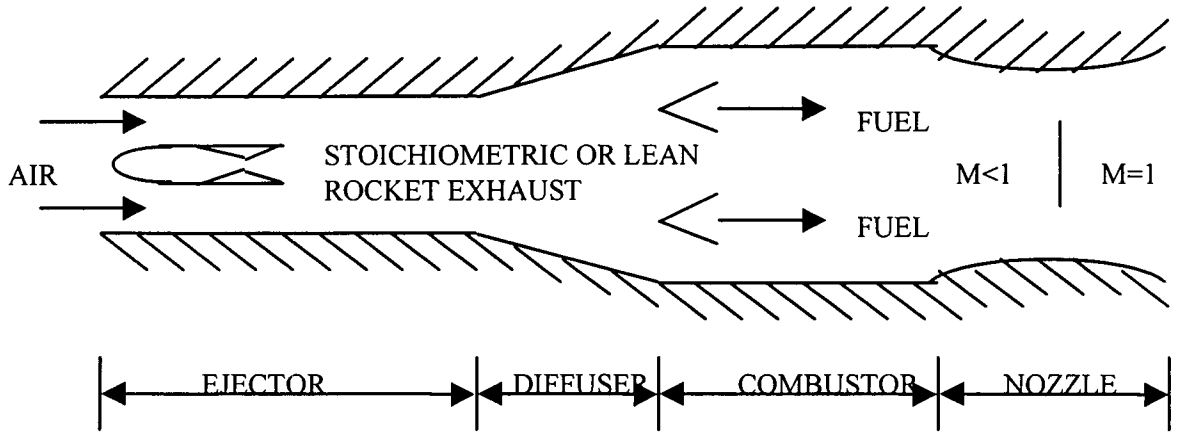

A) Tandem Rocket Ejector-Ramjet

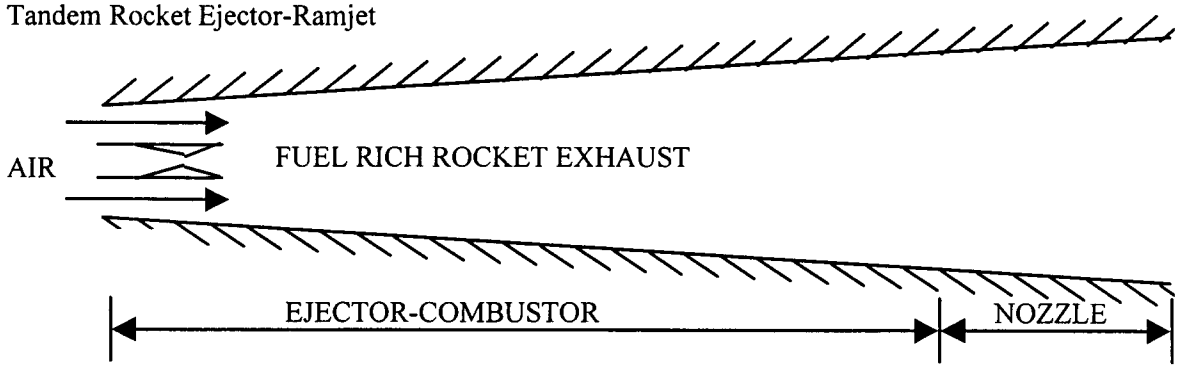

B) Integrated Ejector Combustor

Fig. 1.1. Basic Ejector cycles described by Billig [4].

techniques to quantitatively document the flow characteristics of the rocket-ejector mode of the RBCC engine.

From an RBCC engine design point-of-view, two basic ejector cycles are potentially attractive as noted by Billig [4] and schematized in Fig. 1.1. The first cycle concept includes a sequential inlet/rocket ejector/mixer/diffuser/combustor/nozzle assembly. This is also the cycle that was studied by Odegaard and Stroup. The second cycle concept features a single integrated duct with no physical nozzle that relies on thermal choke to simulate the key features of the first cycle. The experiments reported in the original study investigated both these cycle concepts, whereas the focus of the current study is to further investigate the first concept.

The original study [2] was conducted using a two-dimensional rocket-ejector setup that used a single two-dimensional gaseous hydrogen/gaseous oxygen (GH_2/GO_2) rocket as the ejector. A schematic and photograph of the setup are shown in Figs. 1.2 and 1.3, respectively.

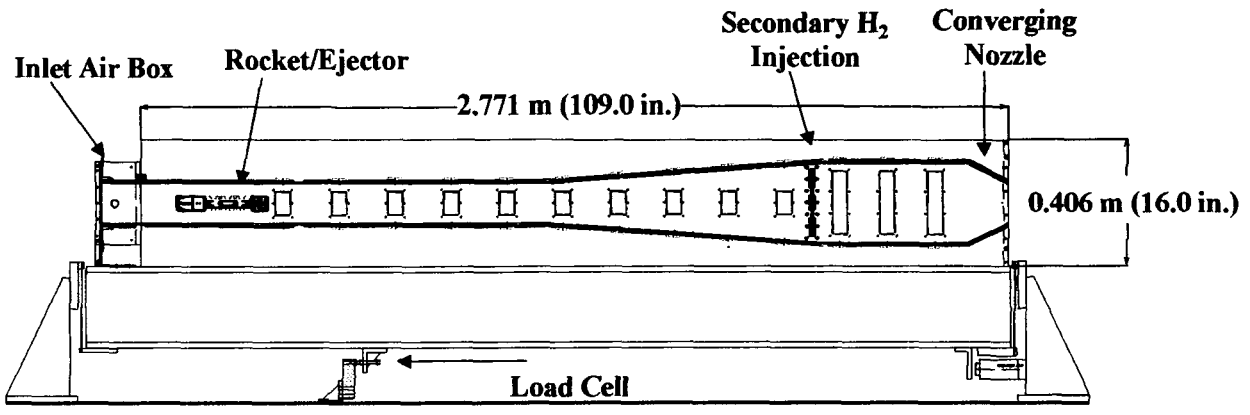

Fig. 1.2. Side view of direct-connect Diffusion and Afterburning (DAB) RBCC test rig developed in the original program. Flow is from left to right.

Experiments of this original study were conducted for the Diffusion and Afterburning (DAB) geometry for both direct-connect (DC) and sea-level static (SLS) configurations. The ejector rocket was operated at mixture ratios of eight and four and at chamber pressures of 500 and 200 psia. Experimental measurements included estimation of the overall system performance obtained through global measurements of wall static pressure profiles, heat flux profiles and engine thrust, and detailed mixing and combustion information obtained through Raman spectroscopy measurements of major species (gaseous oxygen, hydrogen, nitrogen and water vapor).

Based on the success of the earlier program [2], additional research was conducted using the established rocket-ejector facility. The objectives of the additional research, as reported here, were to establish databases for a (a) single rocket ejector that uses JP-7/GO_2 propellants, and (b) twin-rocket ejector that use GH_2/GO_2 propellants. For the first task, the suite of measurements includes rocket ejector duct static pressure profiles, and heat flux profiles, as well as overall engine thrust. These experiments were conducted at the lower rocket chamber pressure of 200 psia. For the second task, two identical rockets were designed, each with one-half the frontal cross-sectional area of the existing single rocket unit. These rockets were designed for 200 psia operation. In addition to the global measurements of static pressure/heat flux profiles and engine thrust, measurements for the twin-rocket configuration also include detailed flowfield measurements of major species.

In this report, the experimental facility and setups are first described in Chapter 2, followed by a description of diagnostic techniques in Chapter 3. Results for the single rocket

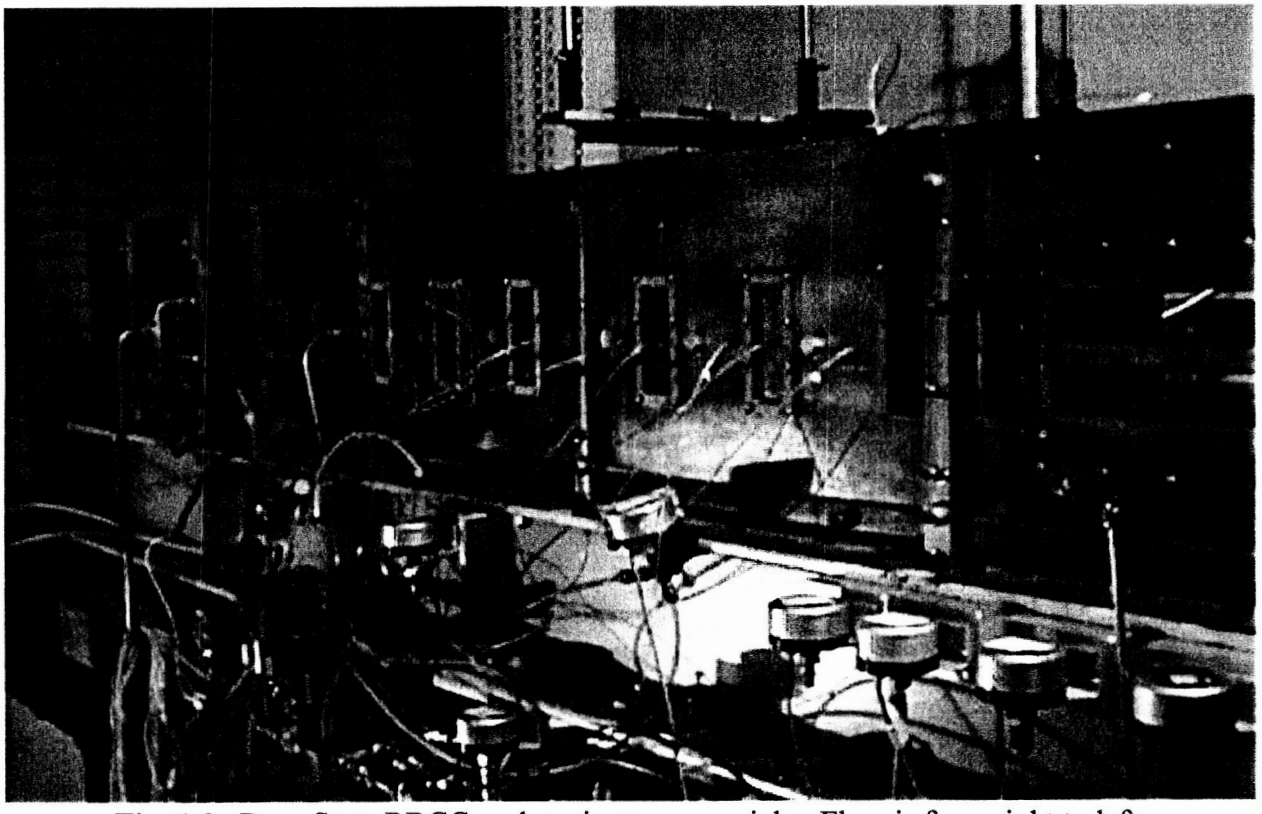

Fig. 1.3. Penn State RBCC rocket-ejector test article. Flow is from right to left.

JP-7/GO_2 and twin-rocket GH_2/GO_2 experiments are presented and discussed in Chapters 4 and 5, respectively.

2. EXPERIMENTAL FACILITY AND SETUP

The RBCC rocket-ejector combustion experiments for both single rocket (JP-7/GO_2) propellants and twin rocket (GH_2/GO_2) were carried out at Penn State's Cryogenic Combustion Laboratory (CCL). This laboratory was established in 1989 to be the flagship facility for Penn State's Propulsion Engineering Research Center (PERC). In this section, the capabilities of the CCL are discussed first. This is followed by a description of the setups used for the two sets of experiments.

2.1. Cryogenic Combustion Laboratory

The CCL is a unique university facility where researchers conduct work on representative rocket engine flowfields. The laboratory is designed based on a similar test cell at the NASA Glenn Research Center (formerly the NASA Lewis Research Center). The CCL, a remotely controlled laboratory, features a control room, diagnostic room and the test cell. The test cell, where the combustion experiment is housed, is isolated from the control and diagnostic rooms with reinforced concrete walls. For experimentation, the test cell's garage door is fully opened and the ventilation turned on to prevent the possible buildup of combustible materials. The diagnostic room located adjacent to the test cell is utilized for situating all the laser-based diagnostics. Optical ports between the diagnostics room and the test cell provide access into the test cell. The control room houses the computer control system that is used for timing the rocket firing. Video cameras with pan features enable remote visualizations of the test room. The operation of the entire system is designed with two levels of safety.

The propellant flowrate capabilities of the CCL are tabulated in Table 2.1. The CCL was initially operable for gaseous oxygen/hydrogen propellants. Liquid oxygen capability was

Table 2.1. Flowrate capabilities of the cryogenic combustion laboratory (CCL).

Propellant	Maximum Flowrate (lbm/s)
Gaseous Oxygen (GO_2)	1
Gaseous Hydrogen (GH_2)	0.25
Liquid Oxygen (LOX)	1
Liquid Hydrocarbon	0.5
Air	4 (can be upgraded to 16)

Table 2.2. Comparison of current rocket ejector and Odegaard and Stroup setups.

	Marquardt *(Areas Divided by 8)*	**Penn State**
Thruster Throat Area, A_t (sq in)	0.274	0.300
Mixer Section Area, A_{mix} (sq in)	14.1	15.0
A_{mix}/A_t --	51.5	50.0
Afterburner Area, $A_{A/B}$ (sq in)	31.75	30
$A_{A/B}/A_{mix}$ --	2.25	2.00
Duct Exit Area, A_{ex} (sq in)	14.4	15.0
Mixer/Combustor Length, L_{mix} (in)	36.0 *(Baseline)*	35.3
Duct Length (without inlet), L_{tot} (in)	107 *(Baseline)*	109

initiated within a year of the laboratory's operation. Liquid hydrocarbon capability was brought on-line three years later. Finally airflow capability was brought on-line in early 1997.

2.2. JP-7/GO_2 Single Rocket Ejector Setup

The JP-7/GO_2 experiments utilized the existing Penn State RBCC hardware and facility [2, 5-7]. The RBCC test rig was designed based on the earlier design by Odegaard and Stroup [3]. The Odegaard and Stroup design was axisymmetric and employed an annular array of rocket/ejectors. The configuration used in the current set of experiments focuses on a 1/8 "sector" slice of the axisymmetric design, maintains the critical area ratios, and converts them into a 2-D geometry. The key geometric parameters defining the current two-dimensional rocket-ejector are compared to those of Odegaard and Stroup in Table 2.2.

Schematics for both direct-connect (DC) and sea level static (SLS) experiments are shown in Fig. 2.1 for the DAB configuration. These configurations differ only in the inlet section: For the DC experiments, air flow (secondary flow) was controlled by a venturi and delivered through a closed inlet box (Fig. 2.1(a)). On the other hand, the SLS configuration (Fig. 2.1(b)) had an open inlet that allowed ambient air to be entrained into the flow path, where flow rates of the entrained air depended on the pumping effect of the rocket-ejector. Details of the two rocket ejector inlets are shown in Fig. 2.2.

The rocket ejector flow path has four sections downstream of the rocket exit plane: a mixer, a diffuser, an afterburner, and a converging nozzle as labeled in Fig. 2.1(a). Throughout the flow path, the internal width was uniform (3 in.) to allow two-dimensional flow field analyses.

The DAB geometry was designed to achieve optimum performance when the rocket was operated at stoichiometric conditions. The hot products from the rocket (primary flow) and the air (secondary flow) mix in the 35 in. long constant area mixer section with internal height of 5 in. The mixed flow, then passes through the diffuser section that was 35 in. in length. The flow path height continuously expands from 5 in. to 10 in. at the end of the diffuser section. Secondary fuel (GH_2) is injected at this axial location from a vertical series of seven 0.1 in. diameter orifices (both sides). The ejected air and the afterburner fuel combust in the constant area afterburner which is 10 in. in height and 18 in. long. Finally, the flow accelerates in the

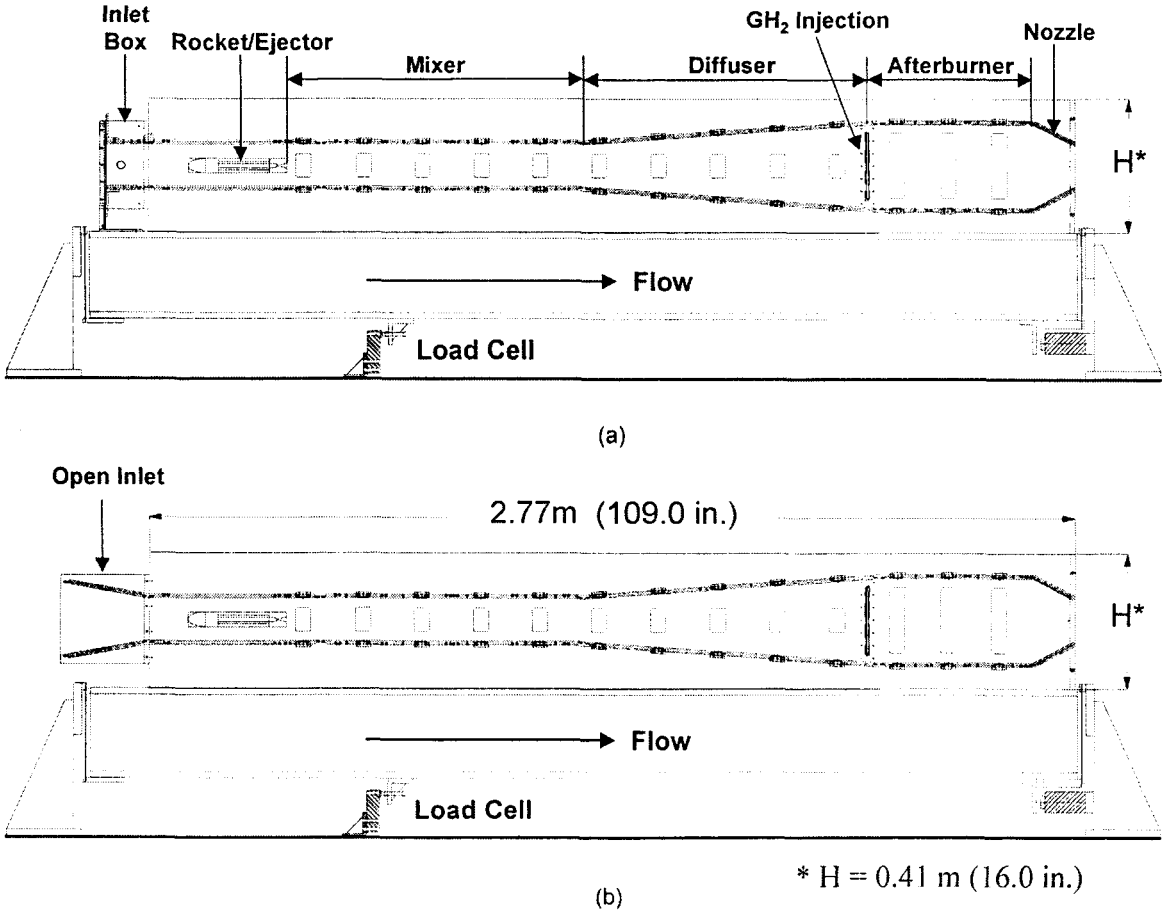

Fig. 2.1. RBCC test rig for the DAB geometry with modifications of the inlet section. (a) direct connect configuration (DC), (b) sea level static configuration (SLS).

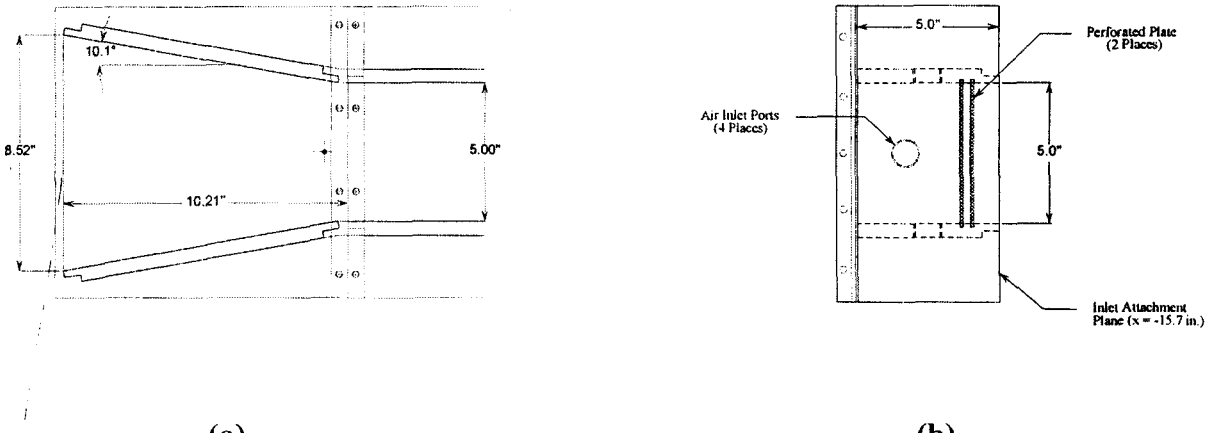

(a) **(b)**

Fig. 2.2. Rocket ejector inlet configurations. (a) Open inlet, and (b) direct connect.

converging nozzle which has a contraction ratio of two. Both the length and the exit height of the converging nozzle are 5 in. The rocket ejector rig is made from oxygen-free high-conductivity (OFHC) copper whereas the joints are supported using stainless steel bars.

The rocket ejector setup features measurement ports for static pressure and heat flux measurements. The entire test rig is mounted on a hanging I-beam to enable thrust measurements using a load cell. Details of all measurements are described in the next chapter.

The rocket was located along the centerline of the flow path at an axial location 4.4 in. downstream from the inlet of the straight section of the air duct. The rocket consisted of a nose cone, an injector, a combustion chamber, and a nozzle as shown in Fig. 2.3. All of the rocket components have rectangular cross sections with an internal width of 3 in., which is the same as the rocket ejector flow path width. Thus, the rocket provides a uniform flow field across the width of the rocket ejector flow path. The total length of the rocket is 11.60 in., whereas the

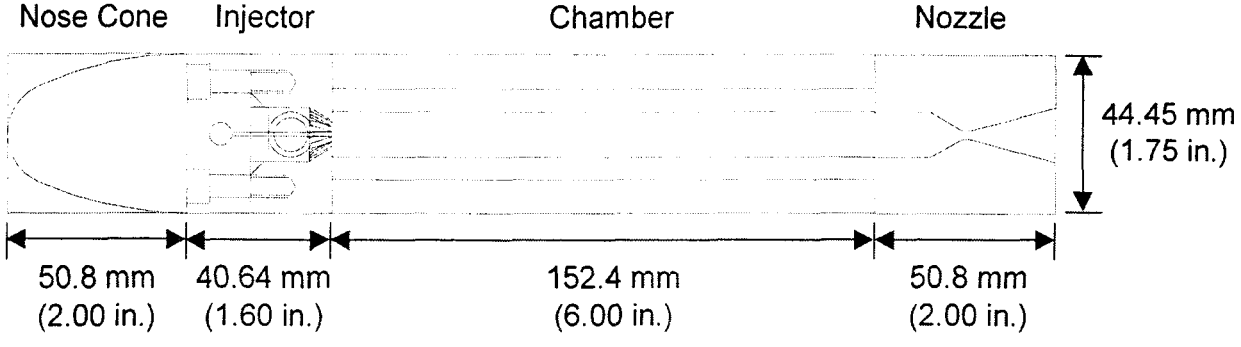

Fig. 2.3. Rocket assembly for JP-7/GO_2 rocket ejector experiments.

Table 2.3. Comparison of static pressures at the rocket exit plane for JP-7/GO_2 and GH_2/GO_2 propellants at stoichiometric mixture ratios.

Pc		JP-7/GO_2		GH_2/GO_2		Difference
MPa	(psia)	kPa	(psia)	kPa	(psia)	%
1.38	(200)	91.9	(13.3)	91.2	(13.2)	0.7
3.45	(500)	104.6	(15.2)	103.1	(15.0)	1.4

internal height of the combustion chamber is 0.5 in. The rocket sections are made from OFHC copper that are supported with bottom and top stainless steel plates.

Two rocket nozzles with expansion ratios of 3.3 and 6.0 are available for chamber pressures of 200 and 500 psia, respectively. The nozzle throat is 0.10 in. tall. The nozzle exit heights are 0.33 in. and 0.6 in. for the two nozzles, respectively. Although the nozzles were designed for GH_2/GO_2 propellants, the static pressure at the exit plane is comparable for JP-7/GO_2 and GH_2/GO_2 operations as summarized in Table 2.3.

An impinging injector as shown in Fig. 2.4 was designed and fabricated for the JP-7/GO_2 rocket-ejector experiments. The injector body and posts (inner tubes) are made of OFHC copper

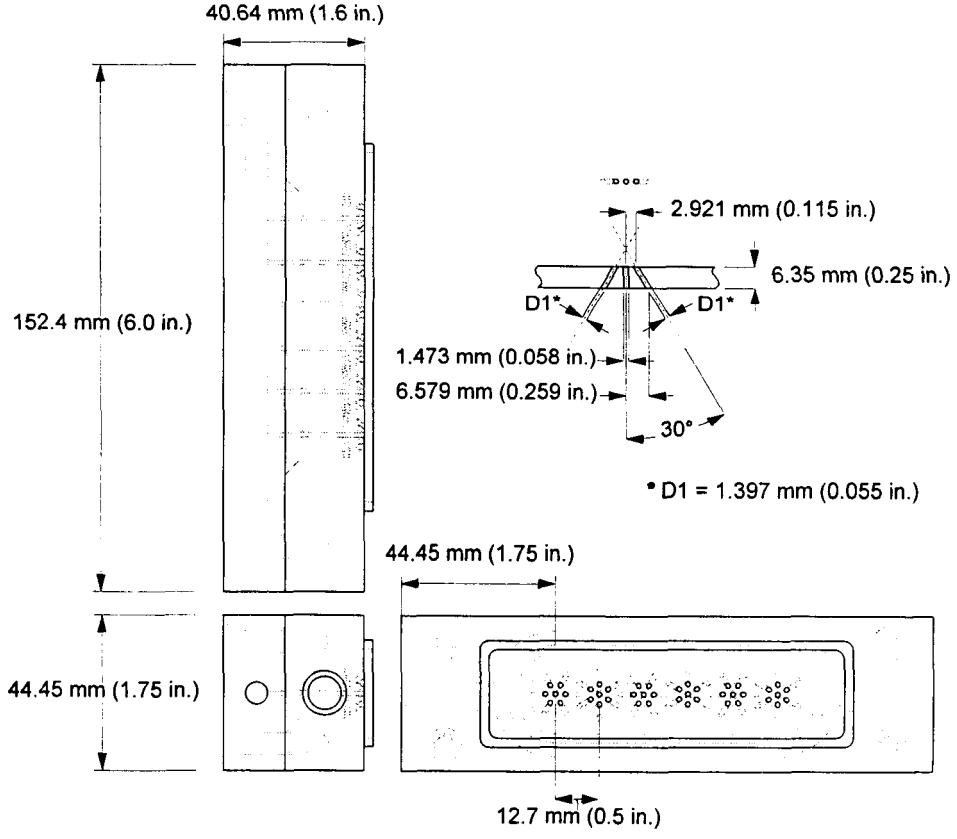

Fig 2.4. Detail of the JP-7/GO_2 injector design.

Table 2.4. Calculated injection velocities.

	JP-7	GO_2
The Number of Orifices per Element	1	6
Orifice Diameter, mm (inch)	1.48 (0.058)	1.40 (0.055)
Injection Velocity at Pc = 1.38 MPa (200psia) m/s (ft/s)	4.3 (14.2)	123.4 (404.7)
Injection Velocity at Pc = 3.45 MPa (500psia) m/s (ft/s)	10.7 (35.1)	121.9 (400.0)
Impinging Angle, degree	---	30

and stainless steel, respectively. The injector consists of six elements that are equally spaced at intervals of 0.5 in. Each element has one straight JP-7 orifice surrounded by six identical GO_2 orifices with an impingement angle of 30°. Calculated injection velocities for the injector are presented in Table 2.4. In the table, injection velocities for both 200 and 500 psia chamber pressure are shown. Note that experiments for only 200 psia rocket chamber pressure were conducted for this phase of the program.

2.3. JP-7/GO_2 Single Rocket Ejector Operating Conditions

The JP-7/GO_2 RBCC rocket ejector experimental series were investigated at six operating conditions (Cases 1 – 6) with the Diffusion and Afterburning (DAB) geometry. The operating conditions were based on earlier single rocket experiments with GH_2/GO_2 propellants [2, 5-7]. All the cases were for a rocket chamber pressure of 200 psia. Table 2.5 characterizes the operating condition for each case qualitatively, whereas the detailed flow conditions are discussed later. In the table, the bypass ratio is defined as the ratio of the air mass flow rate to rocket propellant (JP-7 and GO_2) mass flow rate.

Table 2.5. Overview of the JP-7/GO_2 experimental cases.

Mode	Direct Connect				Sea Level Static	
Case	**1**	**2**	**3**	**4**	**5**	**6**
Rocket Stoichiometry	Fuel-Rich	Fuel-Rich	Stoichiometric	Stoichiometric	Fuel-Rich	Stoichiometric
Bypass Ratio	2.1	2.7	2.1	2.7	Open Inlet	Open Inlet
Afterburner	Off	Off	On	On	Off	On
Overall Stoichiometry	Fuel-Rich	Stoichiometric	Stoichiometric	Stoichiometric	N/A*	N/A*

* Overall stoichiometry of a SLS case depends on the entrained air flow rate.

Two methods of measuring the stoichiometry are introduced to characterize each case: the "rocket stoichiometry" represents the primary combustion (JP-7 and GO_2) in the rocket; the "overall stoichiometry" is determined for the combustion of the rocket exhaust, air, and GH_2 injected into the afterburner.

Cases 1 - 4 are direct-connect (DC) cases. Cases 1 and 2 differ only in the supplied air flow rate. The air flow rates were based on the flight conditions at Mach 1.0 and 1.9, respectively, at P_c = 500 psia operation as discussed later. For Case 1, the overall stoichiometry remained fuel rich while an overall stoichiometric mixture ratio was achieved for Case 2. Cases 3 and 4 are operated at the same bypass ratios as Cases 1 and 2, respectively, with the downstream GH_2 injection to combust all of the oxygen in the rocket-ejector duct.

Cases 5 and 6 are sea level static (SLS) cases where air is entrained through the open inlet by the pumping effect of the rocket ejector, rather than being supplied through the inlet box. The rocket is operated at a fuel rich mixture ratio in Case 5, and operated at the stoichiometric point in Case 6. For Case 6, the same mass flow rate of GH_2 as Case 3 is injected for the afterburner operation. The air flow rates for the SLS cases were calculated after the experiments using a static pressure measurements made in the inlet section.

As mentioned earlier, previous studies conducted at Penn State for GH_2/GO_2 RBCC rocket ejector conditions [2, 5-7] also investigated six cases based on the earlier experimental study of Odegaard and Stroup [3], in which the engine performance was tested at sea level static, and for flight conditions of Mach 1.0 at 9,400 ft and Mach 1.9 at 40,000 ft. For the GH_2/GO_2 RBCC direct connect cases, two air flow rates were selected by running the RAMSCRAM [8] computer program to simulate these flight conditions for a rocket operating at a chamber pressure of 500 psia.

The operating conditions for the JP-7/GO_2 experiments were determined to produce the same rocket and overall equivalence ratios as the GH_2/GO_2 experiments. Matching these conditions allows comparisons to be made between tests that use JP-7/GO_2 and GH_2/GO_2 propellants. The rocket equivalence ratio of unity was used for the GH_2/GO_2 experimental series for Cases 3, 4, and 6, whereas for Cases 1, 2, and 5, the rocket equivalence ratio was chosen to be two. Since one of the objectives of the JP-7/GO_2 experimental series was to reproduce these equivalence ratios, the stoichiometry of the primary propellants are reviewed in this section to

document the rocket O/F selections for this set of experiments. The equivalent chemical composition of JP-7, $C_{10}H_{21}$, was employed for the analysis.

The stoichiometric combustion between JP-7 and oxygen is:

$$C_{10}H_{21} + 15.25\,O_2 \rightarrow 10\,CO_2 + 10.5\,H_2O \qquad [2.1]$$

Hence, the stoichiometric oxidizer to fuel ratio (O/F) becomes,

$$O/F = \frac{15.25\,MW_{O_2}}{MW_{JP-7}} \cong 3.45 \qquad [2.2]$$

where MW_{O2} is the molecular weight of oxygen, 32.00, and MW_{JP-7} is the molecular weight of JP-7, 141.277. The rocket was operated at the stoichiometric O/F = 3.45 for Cases 3, 4, and 6, and O/F = 1.73 for Cases 1, 2, and 5. These O/F ratios correspond to equivalence ratios of one and two respectively, as discussed earlier.

The operating conditions for the JP-7/GO_2 experiments at rocket chamber pressures of (a) 200 psia and (b) 500 psia are shown in Table 2.6. Note that programmatically, only the 200 psia rocket experiments were conducted for this stage of the investigation. Experiments with the rocket operating at 500 psia will be conducted for the next phase of the investigation.

For stoichiometric rocket operation (Cases 3, 4, and 6), the primary propellants are completely consumed, and the rocket exhaust mixes with the secondary air. The mixed gas is decelerated in the diverging (the diffuser) section prior to combustion with GH_2 in the afterburner. Therefore the secondary combustion for Cases 3, 4, and 6 occurs between oxygen in the air and GH_2 in the constant area afterburner section.

In contrast, the secondary combustion for Cases 1, 2, and 5 occurs far upstream of the afterburner section because a fuel rich rocket operation is not the design condition for the DAB geometry. These conditions were run to obtain additional measurements that will be valuable for modelers but do not represent optimum DAB operation. The reactants of the secondary combustion also differ from the stoichiometric rocket operation cases and are composed of the excess fuel from the rocket and the delivered (or entrained) air. Because of the reactant species variation in the secondary combustion, different stoichiometric O/F ratios were used to determine the overall stoichiometry for fuel-rich and stoichiometric rocket operations. Further flow rate and stoichiometry calculations are presented next.

To determine air flow rates, the composition of the rocket exhaust is required for the fuel-rich rocket operation cases (Cases 1, 2, and 5). Relevant mole fractions were obtained by

Table 2.6. Operating conditions: (a) P_c = 1.38 MPa (200 psia) (b) P_c = 3.45 MPa (500 psia).

Pc = 1.38 MPa (200 psia)	Direct Connect				Sea-Level Static	
	Case 1	Case 2	Case 3	Case 4	Case 5	Case 6
Rocket						
O/F	1.73	1.73	3.45	3.45	1.73	3.45
GO_2 Flow Rate kg/s	0.097	0.097	0.121	0.121	0.097	0.121
(lb/s)	(0.214)	(0.214)	(0.267)	(0.267)	(0.214)	(0.267)
JP-7 Flow Rate kg/s	0.056	0.056	0.035	0.035	0.056	0.035
(lb/s)	(0.124)	(0.124)	(0.077)	(0.077)	(0.124)	(0.077)
Equivalence Ratio	2	2	1	1	2	1
Duct						
Air Flow Rate kg/s	0.325	0.416	0.325	0.416	***0.47***	***0.48***
(lb/s)	(0.716)	(0.916)	(0.716)	(0.916)	***(1.03)***	***(1.06)***
GH_2 Flow Rate kg/s	0	0	0.010	0.012	0	0.010
in Afterburner (lb/s)	(0)	(0)	(0.021)	(0.027)	(0)	(0.021)
Overall Equivalence Ratio	1.28	1	1	1	***0.91***	***0.68***

(a)

Pc = 3.45 MPa (500 psia)	Direct Connect				Sea-Level Static	
	Case 1	Case 2	Case 3	Case 4	Case 5	Case 6
Rocket						
O/F	1.73	1.73	3.45	3.45	1.73	3.45
GO_2 Flow Rate kg/s	0.242	0.242	0.299	0.299	0.242	0.299
(lb/s)	(0.533)	(0.533)	(0.660)	(0.660)	(0.533)	(0.660)
JP-7 Flow Rate kg/s	0.140	0.140	0.087	0.087	0.140	0.087
(lb/s)	(0.309)	(0.309)	(0.191)	(0.191)	(0.309)	(0.191)
Equivalence Ratio	2	2	1	1	2	1
Duct						
Air Flow Rate kg/s	0.811	1.038	0.811	1.038	***0.59***	***0.58***
(lb/s)	(1.787)	(2.288)	(1.787)	(2.288)	***(1.30)***	***(1.28)***
GH_2 Flow Rate kg/s	0	0	0.024	0.030	0	0.024
in Afterburner (lb/s)	(0)	(0)	(0.053)	(0.067)	(0)	(0.053)
Overall Equivalence Ratio	1.28	1	1	1	***1.71***	***1.40***

Note: Bold italicized numbers were calculated after the experiments

(b)

running CEA [9] and are summarized in Table 2.7 along with further calculations. The CEA solutions indicate that there exist large percentages of H_2 and CO in the rocket exhaust. Atomic hydrogen also exists in the exhaust in a very small fraction. Thus, H_2 and CO are considered as constituting the excess fuel from the primary combustion in the rocket and, at the same time, the

Table 2.7. Results of the CEA analyses for the fuel rich rocket cases at (a) $P_c = 1.38$ MPa (200 psia) and $P_c = 3.45$ MPa (500 psia).

Product	Molecular Weight	Mole Fraction	Mass Fraction	Mass Flow Rate	
				kg/s	(lb/s)
H	1.01	0.0001	0.0000	0.0000	(0.0000)
H_2	2.02	0.3278	0.0352	0.0054	(0.0119)
H_2O	18.02	0.1844	0.1768	0.0270	(0.0596)
CO	28.01	0.4161	0.6202	0.0948	(0.2091)
CO_2	44.01	0.0717	0.1679	0.0257	(0.0566)
Total	18.79	1.0000	1.0000	0.1529	(0.3371)

(a)

Product	Molecular Weight	Mole Fraction	Mass Fraction	Mass Flow Rate	
				kg/s	(lb/s)
H	1.01	0.0000	0.0000	0.0000	(0.0000)
H_2	2.02	0.3461	0.0371	0.0142	(0.0313)
H_2O	18.02	0.1661	0.1592	0.0608	(0.1340)
CO	28.01	0.3978	0.5929	0.2263	(0.4990)
CO_2	44.01	0.0900	0.2108	0.0805	(0.1774)
Total	18.79	1.0000	1.0000	0.3818	(0.8417)

(b)

fuel for the secondary combustion with air in the duct. The stoichiometric secondary combustion is then represented by:

$$6.76\,H_2 + 8.25\,CO + 7.51\,(O_2 + 3.76\,N_2) \rightarrow 8.25\,CO_2 + 6.76\,H_2O + 28.23\,N_2 \qquad [2.3]$$

Air flow rates are selected so that overall equivalence ratios are 1.28 and 1 for Cases 1 and 2, respectively. The stoichiometric O/F ratio for the secondary combustion is:

$$Stoichiometric\ O/F = \frac{7.51\,MW_{O_2}}{6.76\,MW_{H_2} + 8.25\,MW_{CO}} \qquad [2.4]$$

where MW is the molecular weight of the individual species. The O/F ratios for Cases 1 and 2 were determined from:

$$O/F = \frac{Stoichiometric\ O/F}{Overall\ Equivalence\ Ratio} \qquad [2.5]$$

Thus,

$$\dot{m}_{O_2} = (O/F)\cdot(\dot{m}_{H_2} + \dot{m}_{CO}) \qquad [2.6]$$

The air flow rates were calculated from:

$$\dot{m}_{air} = \frac{\dot{m}_{O_2}}{Y_{O_2}} \qquad [2.7]$$

where Y_{O2} is the mass fraction of oxygen in the air.

$$Y_{O_2} = \frac{MW_{O_2}}{MW_{O_2} + 3.76\,MW_{N_2}} \approx 0.77 \qquad [2.8]$$

The air flow rates obtained from this analysis are summarized in Table 2.6.

For Cases 3, 4, and 6, the primary fuel is consumed completely because the rocket is operated at an equivalence ratio equal to unity. Again, overall equivalence ratios for the Cases 3 and 4 are required to match with the GH_2/GO_2 experimental series [2]. Since the reactants of the secondary combustion for these cases were gaseous hydrogen injected in the downstream afterburner and air, the overall equivalence ratios were determined based on H_2/O_2 stoichiometric O/F = 8.

2.4. GH_2/GO_2 Single and Twin Rocket Ejector Setups

The test setup used for the GH_2/GO_2 Single and Twin rocket ejector was the same as that used for the JP-7/GO_2 experiments described earlier (Figs. 2.1 and 2.2). The setups differ in the rocket designs. For the GH_2/GO_2 Single rocket ejector setup, an extensive set of experiments were conducted and reported in the earlier comprehensive report [2]. Experiments for the earlier program focused on 500 psia Single rocket ejector operation. Experiments were also conducted for 200 psia rocket operation utilizing the same rig. The goal of the current set of experiment is to compare and contrast Single and Twin rocket ejector operation. Consequently, a set of experiments at 200 psia rocket operation (with a newly designed 200 psia rocket nozzle) were first conducted to form an exact basis for comparison with 200 psia Twin rocket ejector operation.

For the Single rocket ejector experiments, the overall rocket assembly shown in Fig. 2.3 was used. However, the injector used for the rocket was not the one shown in Fig. 2.4 but the six-element shear coaxial design shown in Fig. 2.5. The rocket nozzle used was the 200 psia nozzle with a throat height of 0.1 and an exit height of 0.33 in. (area ratio of 3.3) which ideally expands the gas from the chamber pressure down to atmospheric pressure. This 200 psia nozzle was fabricated for the current set of experiments.

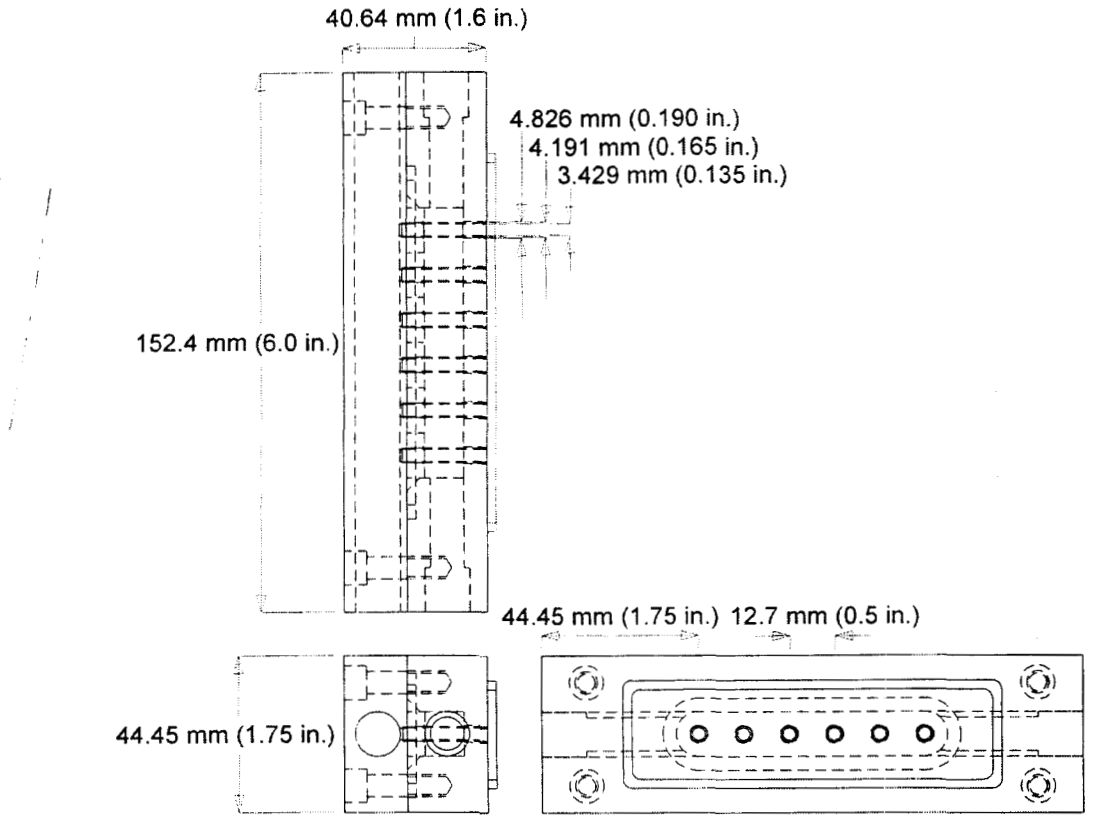

Fig. 2.5 Detail of injector body for Single rocket ejector experiments.

The Twin rocket ejector experiments used two smaller thrusters stacked in the RBCC setup as shown in Fig 2.6. Details of the Twin thruster design can be seen in Fig. 2.7. The incoming air flowed above and below the thrusters, as well as between them. Because of stress and cooling issues, these smaller thrusters were only operated up to a P_c of 200 psia.

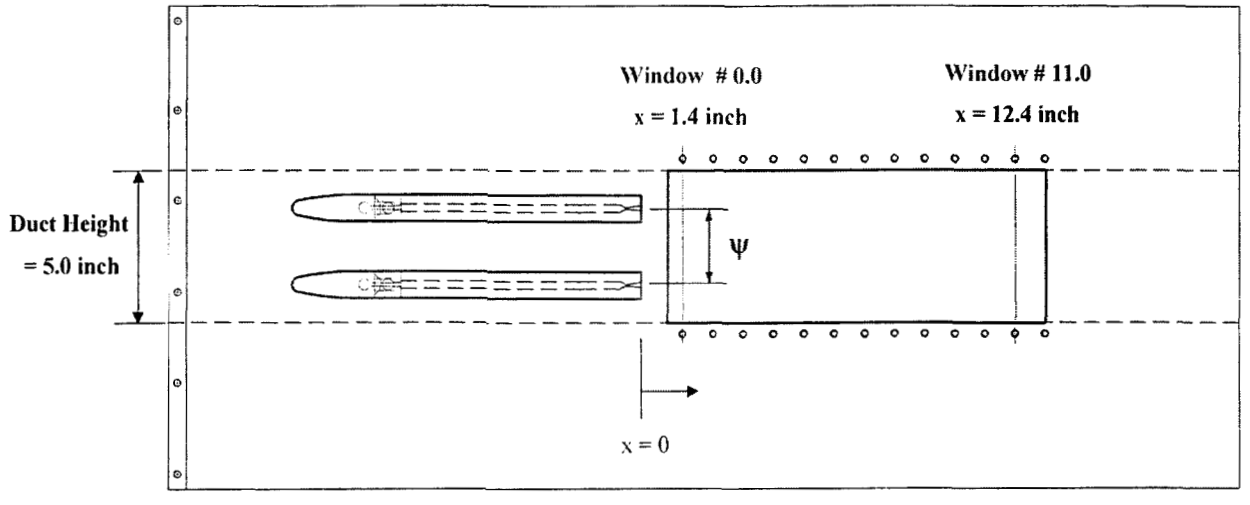

Fig. 2.6. Twin thruster spacing and optical access in the RBCC duct.

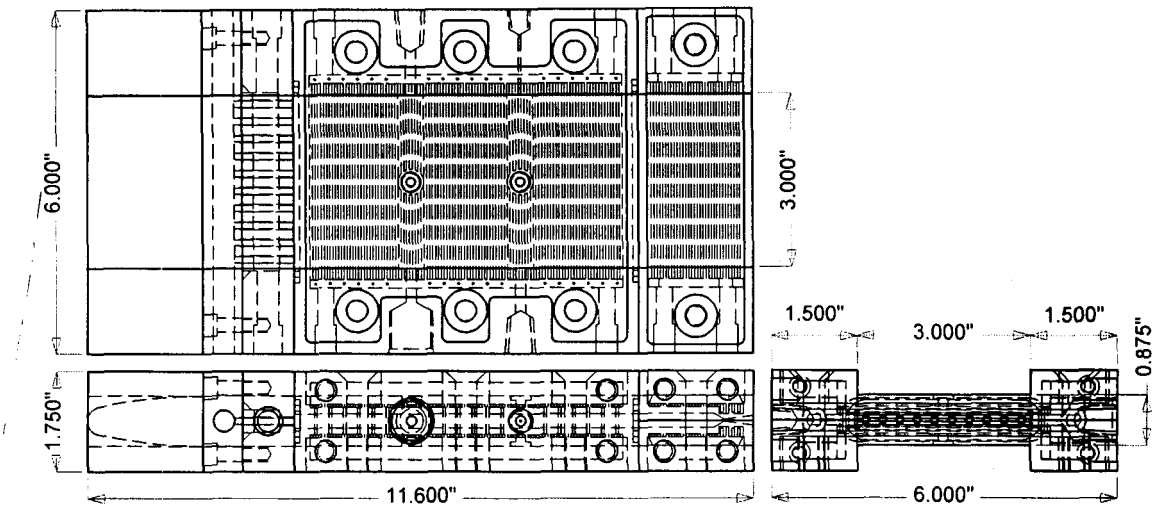

Fig. 2.7. Assembly drawing of single twin-rocket for GH_2/GO_2 propellants.

The blockage area, nozzle exit area, and rocket propellant flow rates of the twin thrusters combined equaled those of the single thruster. Thus a direct comparison of results could be made between the single and twin thruster configurations at a P_c of 200 psia.

Because the flow rate through each twin-thruster was half that of the single thruster, the size of the injector elements was reduced. The elements had the same basic shear coaxial design as the single thruster injector. The GO_2 post inner diameter (ID) was 0.106 in., the fuel annulus I.D. was 0.134 in., and its outer diameter was 0.156 in. In an effort to keep the thruster flow uniform across the duct, ten of these smaller elements were used per thruster. The drawing of the injector is shown in Fig. 2.8. The axial dimensions of the twin thrusters were identical to those of the single thruster. The height dimensions were exactly half those of the single rocket. A torch igniter was mounted to the side of each thruster combustion chamber.

The twin thrusters could be stacked in three different positions within the 5 in. high duct as shown in Fig. 2.9. The thruster centerline-to-centerline distance ("ψ" in Fig. 2.6) could be set at 1.75, 2.50 or 3.25 in. These spacings will be referred to as Twin A, B and C, respectively. Note that in this report, all experiments were conducted for the Twin B ($\psi = 2.50$ in.) configuration. In all cases the thrusters were equally spaced from the centerline of the duct, and their exit planes were at the same axial position ($x = 0$ in.). These thruster spacing options provided a means for studying some of the geometric effects on the pumping and mixing processes. Table 2.8 summarizes the geometric variations that can be achieved at the different thruster spacings.

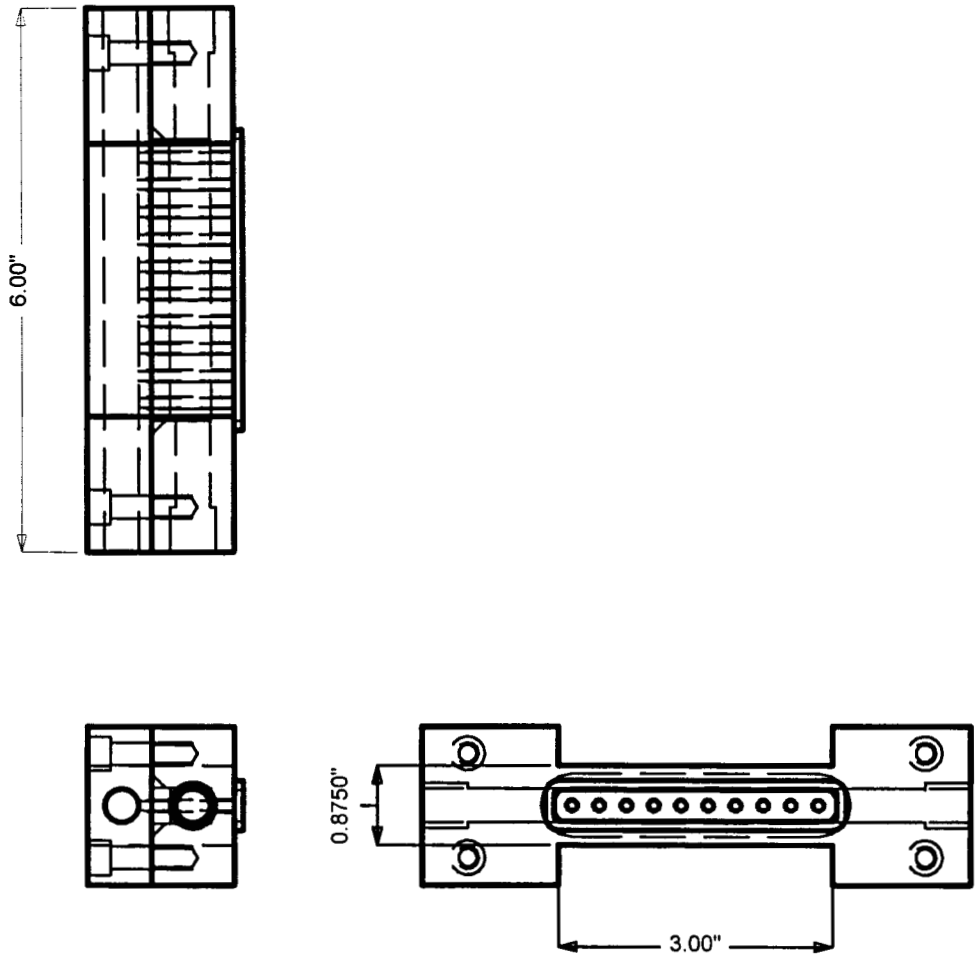

Fig. 2.8 Detail of injector body for Twin rocket ejector experiments.

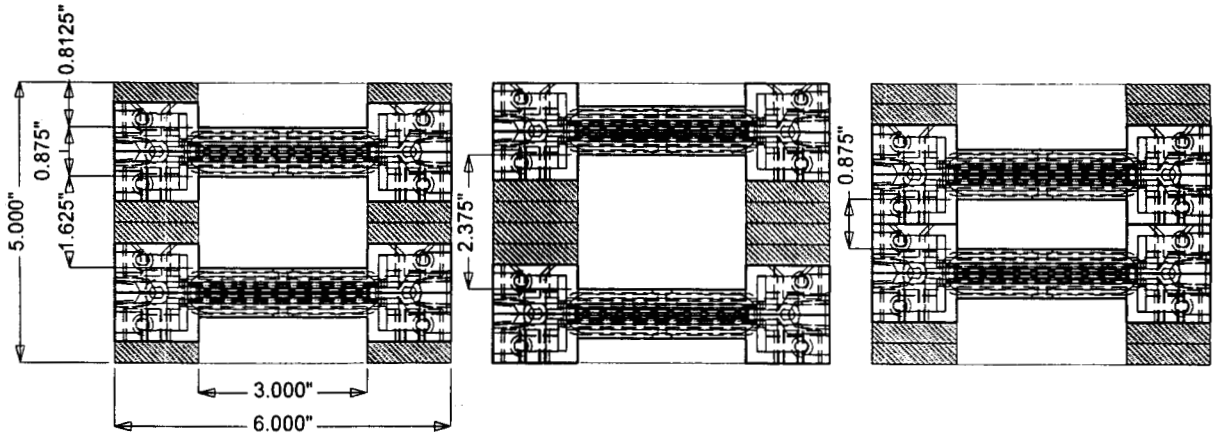

Fig. 2.9. Schematic showing possible twin rocket placements in RBCC duct.

Table 2.8. Summary of twin thruster spacing options.

		Far Spacing	Mid Spacing	Near Spacing
Thruster Centerline-to-Centerline Spacing, ψ	(in)	3.25	2.50	1.75
Nozzle Spacing Ratio, ψ/h	--	19.7	15.2	10.6
Thruster Centerline-to-Wall Spacing	(in)	0.875	1.250	1.625
Total Secondary Flow Area, A_2	(sq in)	9.75	9.75	9.75
Secondary Flow Area (Center), $A_{2,c}$	(sq in)	7.125	4.875	2.625
Secondary Flow Area (Near Walls), $A_{2,w}$	(sq in)	2.625	4.875	7.125
Ratio of Secondary Flow Areas, $A_{2,c}/A_{2,w}$	--	2.71	1.00	0.368

2.5. GH_2/GO_2 Single and Twin Rocket Ejector Operating Conditions

Single and twin thruster tests were conducted at the six operating points detailed in Table 2.9. The air box was installed at the front of the duct for Cases 1-4 (DC), and the open, converging inlet was used for Cases 5 and 6 (SLS). All tests in this study were conducted for rocket chamber pressure of 200 psia and a thruster mixture ratio (O/F) of 4 or 8. The propellant

Table 2.9. RBCC operating conditions for P_c = 200 psia.

	Direct Connect				Sea-Level Static	
	Case 1	Case 2	Case 3	Case 4	Case 5	Case 6
Simulated Flight Mach # ==>	**1.0**	**1.9**	**1.0**	**1.9**	**0.0**	**0.0**
Thruster O/F ==>	**4**	**4**	**8**	**8**	**4**	**8**
Thruster Flows						
Total GO_2 Flow Rate (lb_m/s)	0.188	0.188	0.243	0.243	0.188	0.243
Total GH_2 Flow Rate (lb_m/s)	0.0470	0.0470	0.0304	0.0304	0.0470	0.0304
Duct Flow						
Air Flow Rate (lb_m/s)	0.630	0.807	0.630	0.807	n/a	n/a
Afterburner Flow						
Total A/B GH2 Flow Rate (lb_m/s)	0.0	0.0	0.0184	0.0236	0.0	0.0184

flow rates in each of the twin thrusters were half of the totals stated in the table. Because of the open inlet, the air flow rate for the SLS cases was not controlled. The actual flow rate was measured for each of the sea-level static configurations and cases, and those values are reported in Chapter 5.

3. INSTRUMENTATION AND DIAGNOSTICS

All RBCC combustion experiments were designed to evaluate the rocket-ejector flowfield. Diagnostics were employed to evaluate the static pressure distribution within the airduct, engine heat transfer, total engine thrust, and major species profiles. The following sections describe in detail the PC based static pressure measurement system, the heat flux gauges, the load cell, and the Raman spectroscopy setup used for line measurements of major species profiles within the airduct for the GH_2/GO_2 Single and Twin rocket ejector experiments.

3.1. Flowrate Measurements

Conventional propulsion measurement systems were used in the PERC test facility. The gaseous propellant flow rates were metered with critical flow venturis. The gas pressure and temperature were measured upstream of the venturis (P_1 and T_1), and the resulting mass flow rates were calculated using the choked flow equation. For the direct connect configuration, the flow rate of the air supplied to the duct was also metered with a venturi. Liquid flowrate (JP-7) was controlled in a similar manner using a cavitating venturi.

3.2. Airduct Wall Static Pressure Measurements

The static pressure values along one side and the top wall of the airduct were recorded with a PC based data acquisition system. For the Diffusion and Afterburning (DAB) geometry, sixteen channels were located along the centerline of the top wall and the vertical side wall. Along the top wall, the pressure ports begin upstream of the rocket/ejector and terminate at the airduct nozzle plane. The side wall ports are located slightly downstream of the rocket/ejector nozzle plane and also extend to the airduct exit plane. The data was acquired at 6 Hz and each pressure port has a corresponding transducer. The system lines are equipped with a purge source of N_2 to clear the lines of condensation between runs. The location of each transducer (x, y, z coordinates with the origin at the center of the rocket exit plane) is indicated in Table 3.1.

3.3. Airduct Wall Heat Flux Measurements

Engine heat flux measurements were made for each operational case for both one side wall and the top wall of the airduct. Unlike the 32-channel static pressure system, only five heat flux gauges were available. The complete axial profiles were created by periodically moving the location of the gauges to compile a complete profile at each run condition. The top wall

Table 3.1. Typical static pressure measurement port locations.

Side Wall

Channel	X (inch)	Y (inch)	Z (inch)
1	8.53	0	-1.50
2	13.30	0	-1.50
3	15.53	0	-1.50
4	20.30	0	-1.50
5	22.30	0	-1.50
6	28.30	0	-1.50
7	35.08	0	-1.50
8	42.08	0	-1.50
9	49.15	0	-1.50
10	55.80	0	-1.50
11	62.40	-2.00	-1.50
12	67.32	2.50	-1.50
13	75.30	-2.50	-1.50
14	80.70	2.50	-1.50
15	87.30	-2.50	-1.50
16	92.55	0	-1.50

Top Wall

Channel	X (inch)	Y (inch)	Z (inch)
17	-11.70	2.50	0
18	-7.20	2.50	0
19	-2.70	2.50	0
20	0.65	2.50	0
21	3.90	2.50	0
22	7.90	2.50	0
23	11.15	2.50	0
24	15.80	2.50	0
25	21.80	2.50	0
26	33.80	2.50	0
27	42.39	3.01	0
28	49.12	3.49	0
29	55.11	3.92	0
30	61.09	4.35	0
31	74.35	5.00	0
32	85.85	5.00	0

Table 3.2. Heat flux measurement port locations.

Side Wall

Port	X (inch)	Y (inch)	Z (inch)
A	11.03	0	-1.50
B	18.03	0	-1.50
C	23.80	0	-1.50
D	26.80	0	-1.50
E	33.08	0	-1.50
F	40.08	0	-1.50
G	47.90	0	-1.50
H	54.30	0	-1.50
I	62.40	0	-1.50
J	75.30	0	-1.50
K	80.70	0	-1.50
L	87.30	0	-1.50

Top Wall

Port	X (inch)	Y (inch)	Z (inch)
M	2.90	2.50	0
N	8.90	2.50	0
O	11.90	2.50	0
P	20.30	2.50	0
Q	30.30	2.50	0
R	37.30	2.64	0
S	44.30	3.15	0
T	51.30	3.65	0
U	58.30	4.15	0
V	65.30	4.65	0
W	72.30	5.00	0
X	78.30	5.00	0
Y	84.30	5.00	0

locations correspond to the window locations. The top quartz window was replaced with a threaded copper blank to accept a heat flux gauge. The side wall locations were not at window locations and were also always along the airduct vertical centerline. The gauges were 0.5 in. Gardon type units that acquired heat flux data at 200 Hz. The heat flux measurement locations are summarized in Table 3.2.

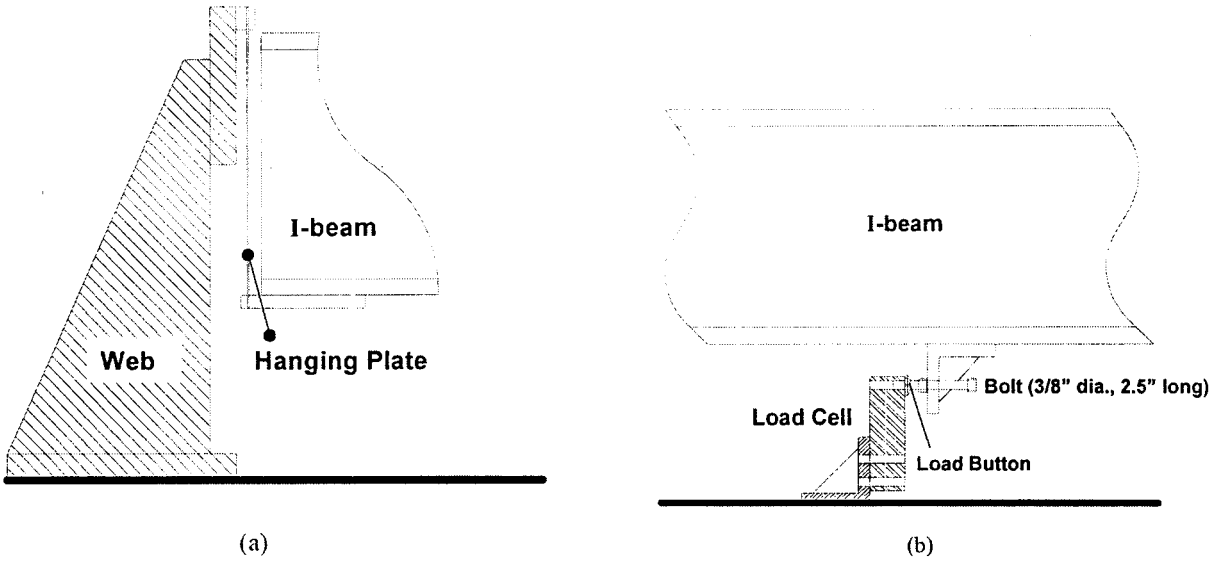

Fig. 3.1. Thrust measurement setup. (a) End of the I-beam and (b) load cell.

3.4. Engine Thrust Measurements

A calibrated load cell with a full scale range of 1000 lbf was used to measure the thrust during each firing. The entire RBCC test rig is mounted on an I-beam. The I-beam is bridged to a fixed web by a metal plate on each side as shown in Fig. 3.1. This mounting method provides a "hanging" condition to the I-beam and allows the measurement of thrust in terms of displacements of the I-beam using the load cell, which is mounted underneath the I-beam. The load cell was manually pre-loaded at the beginning of a day to provide a good mechanical connection. Signals (in volts) were acquired at 50 Hz and scaled to thrust (37733.0 lbf/volt) using the available LabVIEW software. The scaling factor was based on the calibration of the system.

3.5. Ejected Air Flow Rate Measurements

For SLS conditions, viz. Cases 5 and 6, the ejected airflow rate was estimated from a pressure differential measurement between a port in the inlet section and atmospheric pressure. The pressure measurement location is shown in Fig. 3.2. The port is located 9.67 in. downstream of the entrance plane of the open inlet (labeled as Location 3). The pressure differential, ΔP, was measured using a high accuracy pressure transducer. The ejected mass flowrate was then calculated using Bernoulli's equation and the assumption of one-dimensional flow.

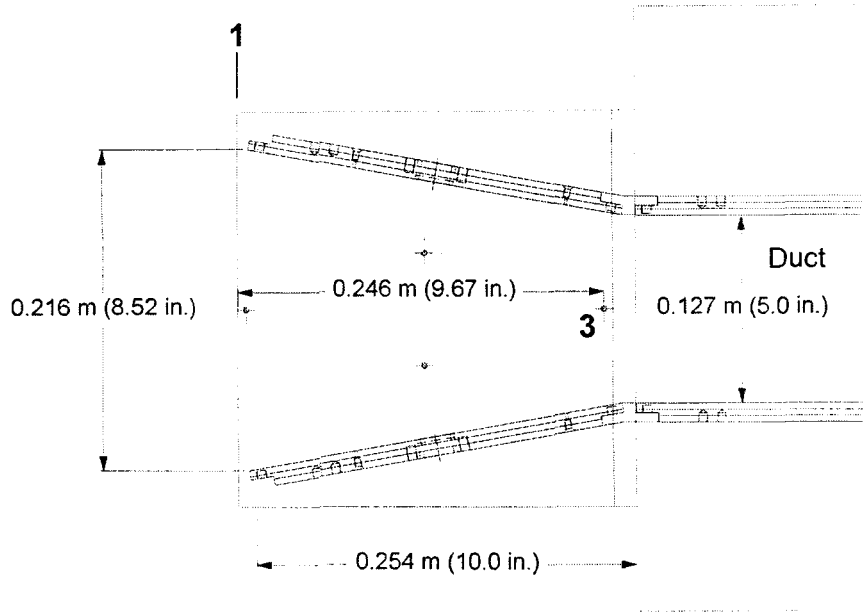

Fig. 3.2. Open inlet (SLS) showing pressure transducer location (labeled as "3") for ejected air calculations.

3.6. Raman Spectroscopy Species Measurements

The optical system used to deliver laser light to the test article is shown in Fig. 3.3. A frequency-doubled Spectra-Physics GCR-200 Nd:YAG laser (532 nm) is used to produce Raman scattering in the RBCC flow field. This laser operates at 10 pulses per second, with pulse energies on the order of 600 mJ per pulse. A Lightwave Injection Seeder in the laser is used to produce laser line widths on the order of 0.003 cm^{-1}. A beam splitter (33% reflection, 67% transmission) and a series of mirrors (M1-M3) converts the 10 nanoseconds (ns) laser pulses into a series of three overlapping pulses that is approximately 30 ns long. By distributing the pulse energy over a longer time period, more total energy is delivered to the probe volume while remaining below the damage threshold of the access window in the duct. A quartz flat is used to reflect a small percentage of the pulse energy into a laser power meter (Molectron Model J50). The resulting average laser pulse energy readings are used to normalize the Raman signal for each of the calibration and hot-fire runs. The laser beam is focused with a 1.0-meter focal length lens (L1) before it passes through the access window at the top of the RBCC duct. An extension tube, approximately 18 in. long and attached to the top of the duct, positions the window far enough away from the beam focal point to prevent damage to the window. A beam dump installed at the bottom of the duct minimizes stray laser light reflections in the duct. The laser

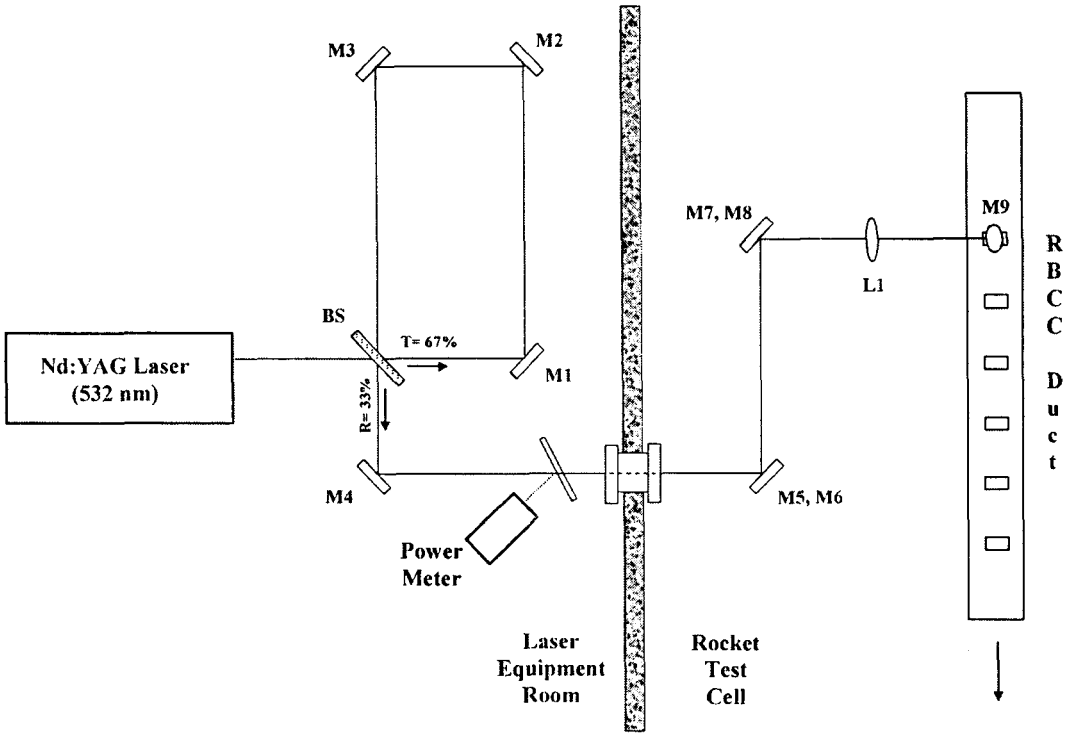

Fig. 3.3. Laser optical system.

beam can be routed to any of the access windows on the top wall of the duct, allowing Raman measurements to be made at a number of axial positions.

The Raman signal collection system is shown schematically in Fig. 3.4. The probe volume is a vertical line approximately 0.040 inches in diameter that passes through the center of the duct. The signal collection optics are mounted horizontally, normal to the flow axis. A Princeton Instruments intensified charge coupled device (ICCD) camera with a two-dimensional array (576 x 384 pixels) is used to image the probe volume through an access window on the duct sidewall. The camera has 14 bits of resolution, providing a dynamic range from 0 to 16,383 counts. The ICCD array is binned 4 x 4, and the active array size is reduced to 144 vertical superpixels by 20 horizontal superpixels. The resulting spatial resolution is ~0.030 in. per superpixel in both directions. The field of view of the access window is 0.4 in. wide by 4.8 in. high, which allows Raman measurements to be made across nearly the entire 5-inch duct height. A Nikon 50 mm lens with the aperture set at f/1.2, collects the light from the probe volume. Narrow bandpass filters are alternately mounted to the camera lens, allowing Raman signal to be collected from one of the major combustion gas species per test. Table 3.3 provides the spectral characteristics of these bandpass filters. A pulse generator (Princeton

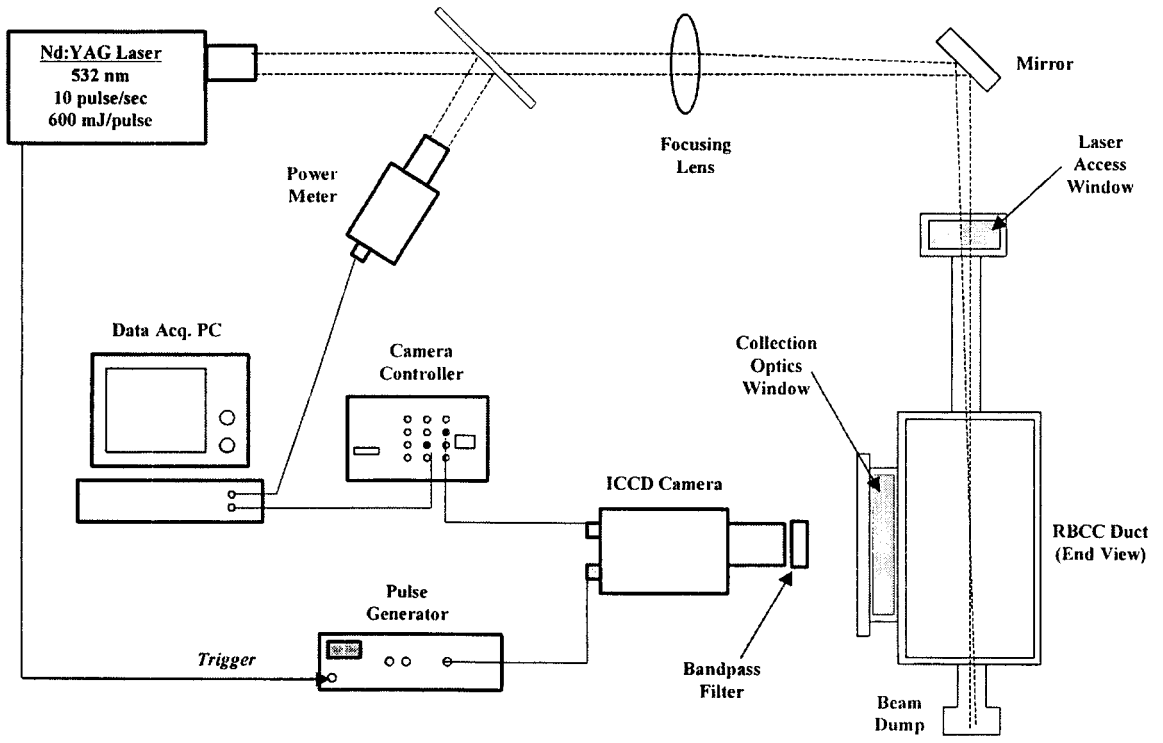

Fig. 3.4. Raman signal collection system configuration.

Instruments Model PG-200), which is triggered by the laser, provides the camera with a gate width of 50 ns. The data transfer rate of the camera controller (Princeton Instruments Model ST-138S) is 100 kHz, fast enough to allow images to be collected on every laser pulse.

The relationship between the number density (n_i) and the measured Raman signal (S_i) for species "i" is given by [10]:

$$S_i = E_l \cdot n_i \cdot K_i \cdot f_i(T) \qquad [3.1]$$

where E_l is the incident laser power, K_i is a constant that depends on the collection efficiency of the optics and the Raman cross section of species "i", and $f_i(T)$ is the bandwidth factor, which is

Table 3.3. Bandpass filter spectral characteristics.

Species	Stokes-Q Branch Peak Wavelength (nm)	Bandpass Filter Peak Wavelength (nm)	Filter Bandwidth [FWHM] (nm)	Filter Peak Transmission (%)
Oxygen	580	581.2	8.5	53.5
Nitrogen	607	608.0	9.4	68.0
Water	660	661.3	9.7	57.8
Hydrogen	681	681.0	9.7	56.4

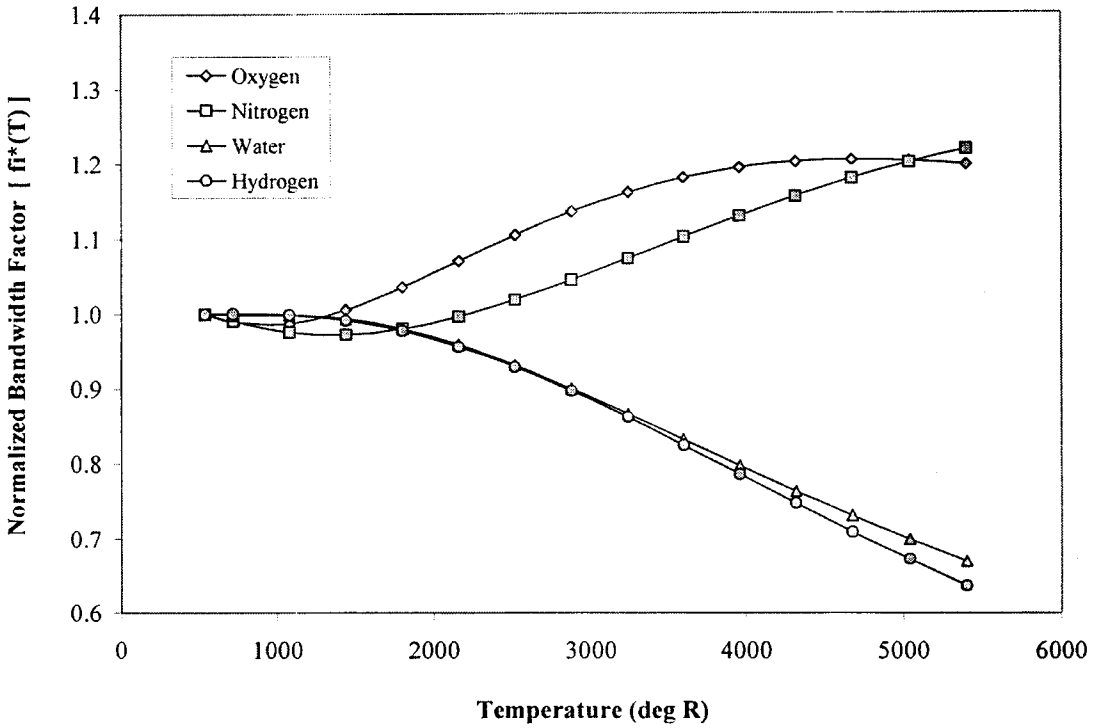

Fig. 3.5. Bandwidth factors for the major gas species.

a function of temperature, species and filter bandwidth. Rearranging equation 3.1 and applying the ideal gas equation of state leads to an expression for the mole fraction of each species (Y_i):

$$Y_i = \frac{P_i}{P_t} = \frac{S_i}{E_l \cdot K_i \cdot f_i(T)} \cdot \frac{R_u \cdot T}{P_t} \qquad [3.2]$$

where P_i is the partial pressure of species "i", P_t is the local static pressure of the system, R_u is the universal gas constant, and T is the absolute temperature.

The calibration constants (K_i) are determined each test day. For N_2, O_2, and H_2, a trickle flow of each pure gas is sequentially put through the duct at ambient pressure and temperature. Raman signal data is collected for each species in turn. Since each gas is pure, the mole fraction is 1.0 and Equation 3.2 can be solved for the calibration constant:

$$K_i = \frac{S_i}{E_l \cdot f_i(T)} \cdot \frac{R_u \cdot T}{P_t} \qquad [3.3]$$

Since water can not be calibrated this way, its K_i values are scaled from the nitrogen values using a scaling constant (B'):

$$K_{H2O} = B' \times K_{N2} = 1.70 \times K_{N2} \qquad [3.4]$$

The value for B' was determined through a series of hydrogen/air premixed burner tests where the equilibrium mole fraction of each of the combustion products was known.

The bandwidth factor, $f_i(T)$, is determined for each species from theoretical Raman signal strength calculations [11]. Figure 3.5 shows the bandwidth factor functions that are used in this study. A polynomial curve fit for each species' bandwidth factor as a function of temperature is used in the data reduction scheme. Since the bandwidth factors are dependent on wavelength, the same functions cannot be used for experiments with different optical characteristics. The functions must be determined for a specific optical configuration.

Approximately 100 steady-state, hot-fire data frames were collected for each species at one operating condition and one window location. An average value of S_i for each species is calculated from these individual data frames at each of the 144 vertical pixel locations. Using the assumption that the only species in the flow field with significant mole fractions are H_2, O_2, N_2 and H_2O lead to the equation required for closure of the calculations:

$$\sum_{i=1}^{4} Y_i = 1 \qquad [3.5]$$

An iterative procedure is then used to solve the five equations for the five unknowns (Y_{H2}, Y_{O2}, Y_{N2}, Y_{H2O} and T) at each pixel location.

4. JP-7/GO_2 ROCKET EJECTOR RESULTS

This chapter describes the JP-7/GO_2 RBCC rocket ejector results for the Diffusion and Afterburning (DAB) configuration. Results include static pressure and wall heat flux profiles, and overall engine thrust. The rocket was operated at a chamber pressure of 200 psia for both direct-connect (DC) and sea level static (SLS) cases. Target flow rates of all the experimental cases were previously discussed in Chapter 2 (see Table 2.6).

4.1 Static Pressure Measurements

Static pressure profiles for the direct connect (DC) experiments for a rocket chamber pressure of 200 psia) are shown in Fig. 4.1. In general, the axial profiles of static pressure along the top and side walls are the same, except near the rocket exit plane where the side wall data points are distributed in a more random manner. This is a region where the two flows, the supersonic rocket exhaust (the primary flow) and the subsonic air flow (the secondary flow), mix as illustrated in Fig. 4.2. Since the side wall measurements were performed along the center line of the rocket, a difference between the side and top wall measurements near the rocket exit represents a pressure difference between the primary and secondary flows due to the shock structure in the supersonic rocket exhaust. This difference is maintained until a significant amount of mixing has occurred between the two flows.

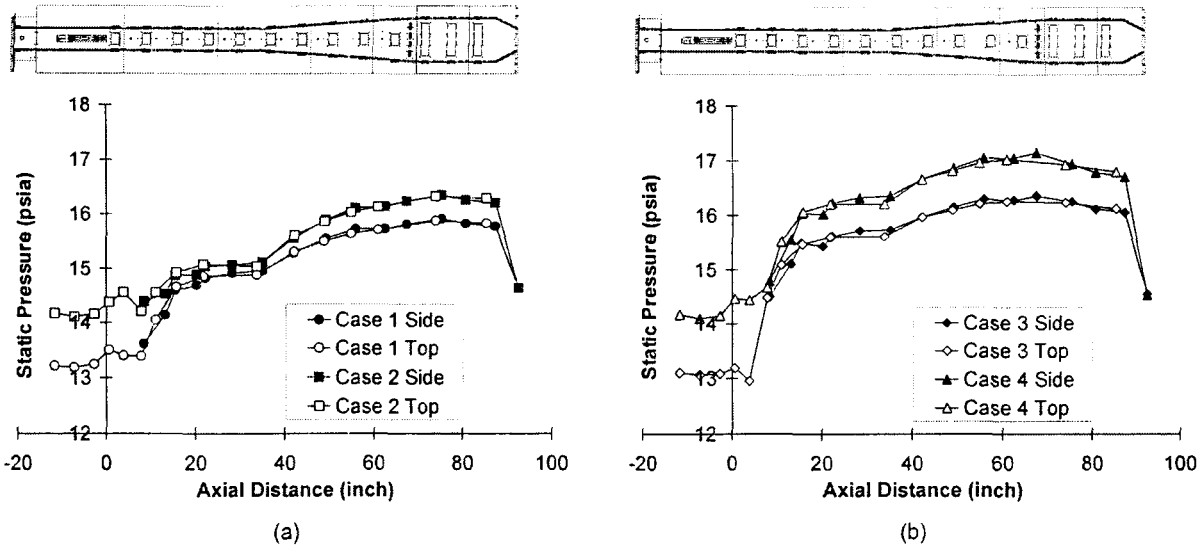

Fig. 4.1. Static pressure profiles for DC cases at $P_c = 200$ psia. (a) fuel-rich rocket cases and (b) stoichiometric rocket cases.

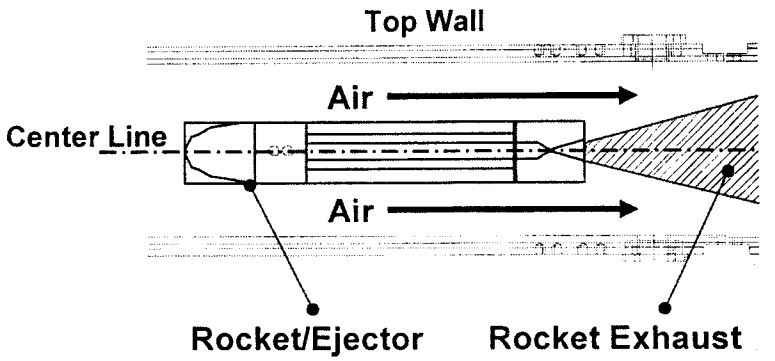

Fig. 4.2. Primary and secondary flows near the rocket exit.

The air flow rate is one of the factors that determines the static pressure level in the duct. The effect of the air flow rate appears as offsets of the pressure profiles shown in Fig. 4.1; a higher air flow rate results in a higher static pressure level throughout the entire duct. This air flow rate effect is isolated in Fig. 4.3 to clarify the issue. For the results shown in Fig. 4.3, the air flow rates were increased by 30% and 50% while other conditions remained the same as Case 4. Figure 4.3(b) shows the axial variation of the air flow effect in terms of static pressure. The increase in the air flow rate causes the static pressure to rise more significantly in the upstream region. On the other hand, the static pressure rise remains approximately constant beyond the axial location x = 20 in., where the mixing of the primary and secondary flows is complete. Despite the axial air flow effect variation, the ratio of the pressure rise at two air flow rates remains constant throughout the duct. The last data point is an exception since it is located at the duct exit plane. For example, the average increase beyond x ~ 20 in. is approximately 6% with 30% air flow rate increase, while it is ~ 10% with 50% air flow rate increase. Thus, the ratio of the static pressure increases becomes 0.6, and this is the same as the ratio of the increase in the air flow rate, which is 0.6 (30% to 50%). In brief, the increase in static pressure is proportional to the amount of the air flow that is applied regardless of the axial location.

The stoichiometry of the primary combustion in the rocket is another factor that affects the static pressure profile. The static pressure levels throughout the duct are higher for the stoichiometric rocket cases (Cases 3, 4 and 6) than for the comparable fuel-rich rocket cases

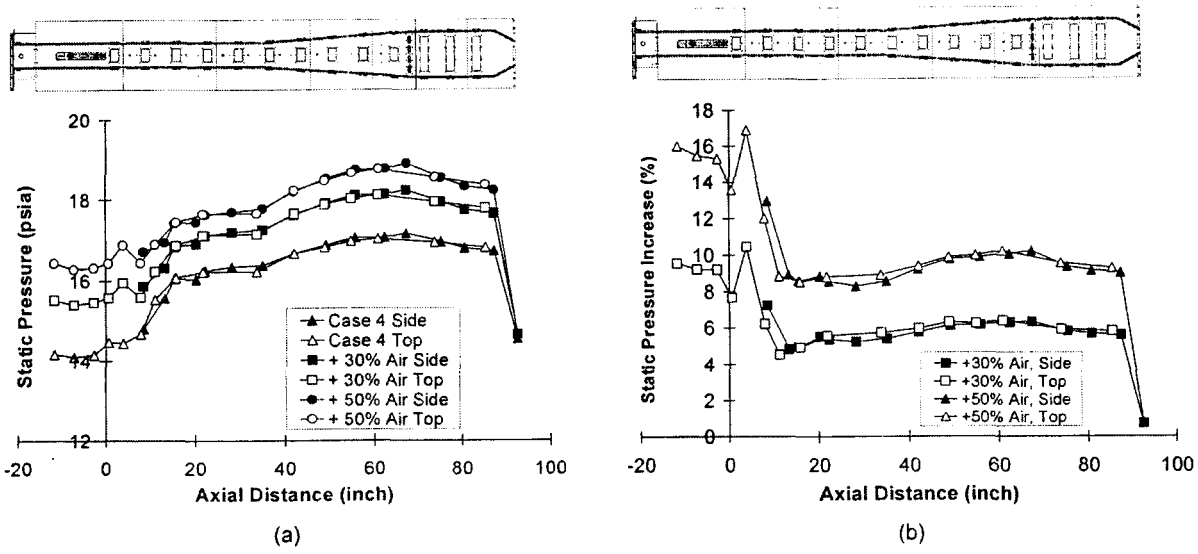

Fig. 4.3. Effect of air flow rate on static pressure profiles at P_c = 200 psia for Case 4 conditions. (a) static pressure profiles at various air flow rates and (b) increase in static pressure.

(Cases 1, 2 and 5). This effect of the rocket stoichiometry on the static pressure profile can be observed in Fig. 4.1.

The static pressure profiles of the sea level static (SLS) cases are shown in Fig. 4.4. For the stoichiometric rocket case (Case 6), the static pressure rises as the primary and secondary flows mix in the mixer section until the point where significant mixing has occurred (x ~ 20 in.). Once the mixing has reached near completion, the static pressure level stays constant in the mixer section. The mixed fluid, then, enters the diffuser section, in which the static pressure

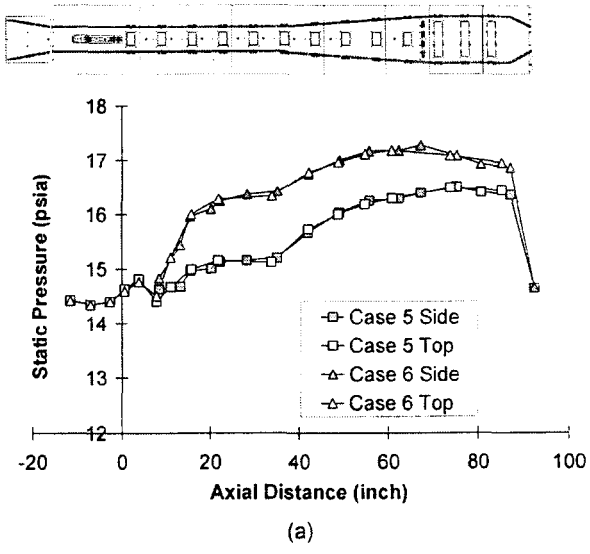

Fig. 4.4. Static pressure profile for SLS cases at rocket P_c = 200 psia.

increases due to flow deceleration. GH_2 is injected at the end of the diffuser section. The heat addition due to the secondary combustion in the afterburner results in lowering of the pressure. However, the secondary combustion tends to raise the back pressure throughout the duct. Thus the RBCC engine can be operated at a higher static pressure level, a desirable operating condition for a combustion device, with the afterburner operational.

The significant difference between the stoichiometric and fuel rich rocket operation cases (Cases 5 and 6) is the level of the static pressure. As discussed above, it is higher for the stoichiometric rocket operation case because of the afterburner operation. The pressure rise in the mixer section also differs due to the rocket stoichiometry. Since the secondary combustion between excess fuel and the air occurs in the mixer section when the rocket is operated at a fuel rich O/F, the resulting heat release disturbs the pressure rise in this region. The constant pressure profile observed in the afterburner section for the fuel rich rocket operation case occurs because no additional combustion takes place. At both rocket stoichiometries, the flow is accelerated through the converging nozzle so that the static pressure drops to atmospheric pressure at the exit plane. The general trend of the static pressure profile is the same for DC cases (Fig. 4.1).

4.2. Heat Flux Measurements

Heat flux profiles for the DC cases (Cases 1–4) at the chamber pressure of 200 psia are shown in Fig. 4.5 for both side and top walls. The heat flux values throughout the duct are

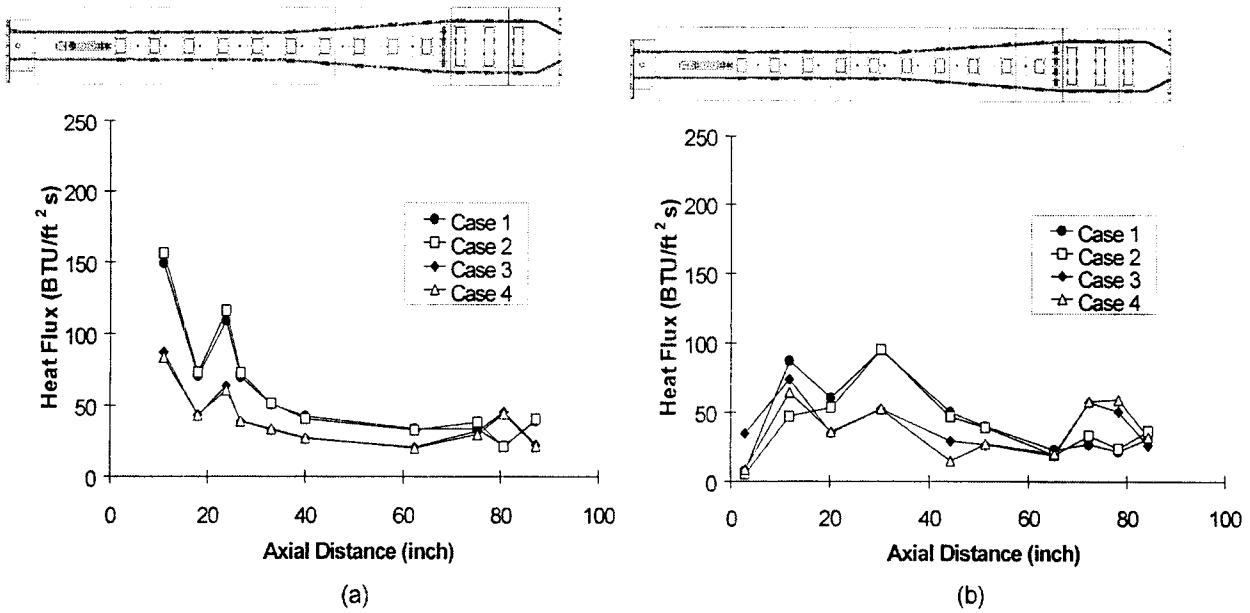

Fig. 4.5. Heat flux profiles for DC cases at $P_c = 200$ psia. (a) Side wall measurements and (b) top wall measurements.

generally higher for the fuel rich rocket cases (Cases 1 and 2) than for the stoichiometric rocket cases (Cases 3 and 4). These higher heat fluxes are due to the heat release from the secondary combustion between excess fuel in the rocket exhaust and air in the duct. An exception to this trend is in the afterburner, at the axial location of approximately 80 in., where GH_2 was injected for Cases 3 and 4. The resulting combustion in the afterburner causes an increase in heat flux. For all of the DC cases, the highest side wall heat flux occurs at the measurement port closest to the rocket exit. Since the side wall measurements are made along the centerline of the rocket, the heat fluxes should be the highest before the hot products of the primary (rocket) combustion has mixed with the air flow (i.e., near the rocket exit plane). On the other hand, the peak heat flux values along the top wall occur 10-30 inches downstream of the rocket exit plane. These peak values roughly correspond to the axial locations where the hot products of the primary combustion have mixed with the air and spread out to the top and bottom walls.

Heat flux profiles for the SLS cases (Cases 5 and 6) are shown in Fig. 4.6. for both side and top walls. In general, the trends of the SLS heat flux profiles (Fig. 4.6) are similar to those of the DC profiles (Fig. 4.5). However, the peak point of the top wall heat flux profiles ($x \sim 20$ in.) is much clearer for SLS cases (Fig. 4.6(b)) compared to DC top wall heat flux profiles (Fig. 4.5(b)). The side wall heat flux profiles of the SLS cases (Fig. 4.6(a)) also show smoother downward trend than DC cases (Fig. 4.5(a)). Both side and top wall heat flux profiles for all of the DC cases dip at $x \sim 20$in.

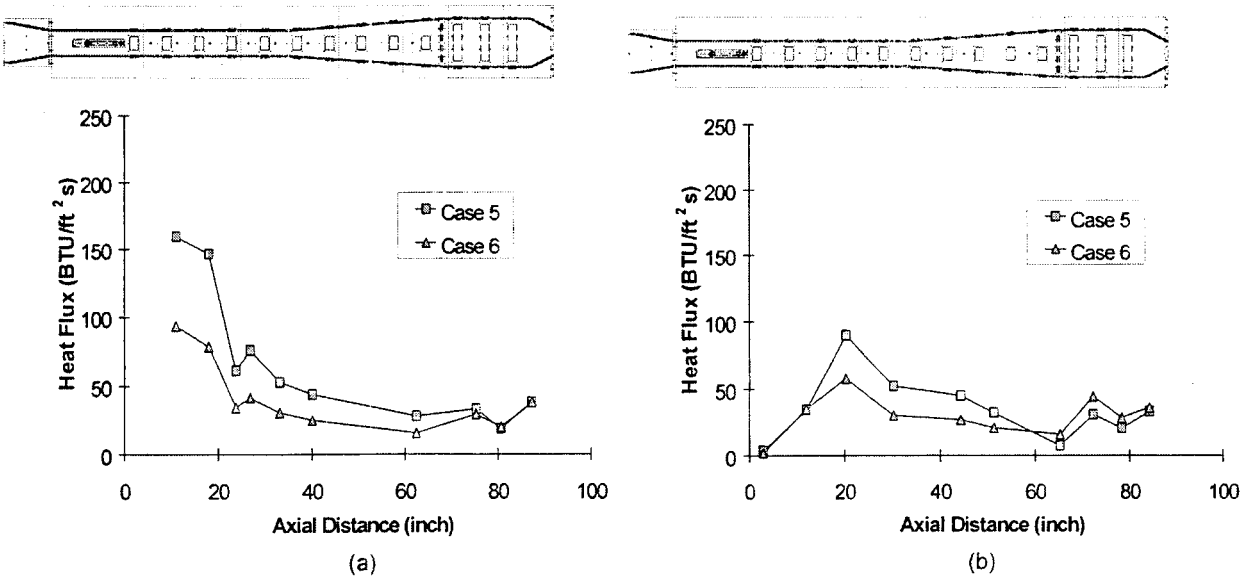

Fig. 4.6. Heat flux profiles for SLS cases at $P_c = 200$ psia. (a) Side wall measurements and (b) top wall measurements.

The heat sources were the same for both DC and SLS cases: the primary combustion in the rocket, and the secondary combustion in the duct. Heat flux profiles of the SLS cases (Fig. 4.6) appear to reflect the combustion and mixing characteristics in the RBCC flow. For the side wall, the heat flux profile should have continuous downward trend since the primary combustion is the only heat source for the major portion of the flow path. A variation of the profile trends is expected at X ~ 70 in. depending on whether the afterburner was operated or not. A top wall heat flux profile should have its peak a little downstream of the rocket exit plane since it takes some axial distance for the rocket exhaust gas to reach the top wall. Again, a variation due to the afterburner operation is predicted for the top wall profiles at the axial location corresponding to the afterburner.

4.3. Thrust Measurements

An example of the raw voltage versus time data for thrust measurements is shown in Fig. 4.7. A moving average of 50 samples is also indicated in the figure. The averaging procedure reduces the level of noise while maintaining the magnitude of the data. The average thrust is obtained from the difference in load cell voltage readings at steady state during the hot fire (t ~ 6 s) and after the firing (t ~ 9 s), and the calibration.

Average thrust value for each case is shown in Fig. 4.8 where labels C1–C6 denote Cases 1–6. The thrust increases as the air flow rate increases. Cases that the rocket operates at an

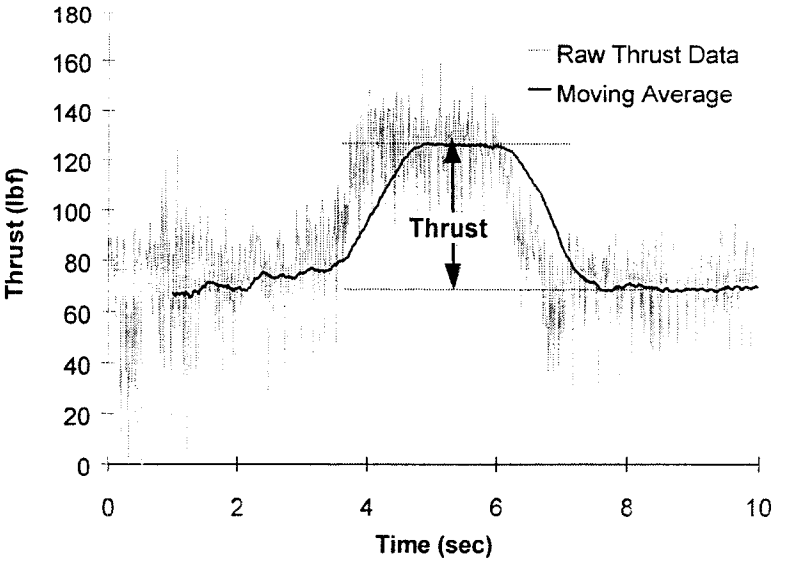

Fig. 4.7. Example of raw thrust data and its moving average.

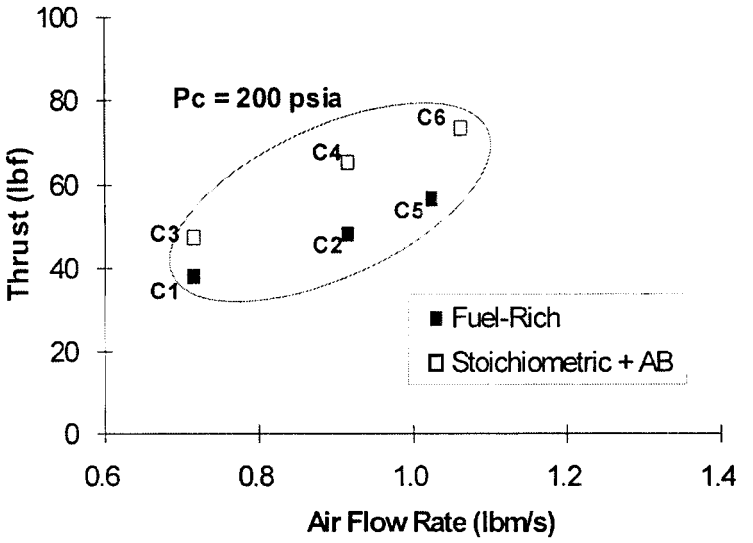

Fig. 4.8. Average thrust values versus air flow rate.

equivalence ratio of unity and use the afterburner (Cases 3, 4 and 6) had higher levels of thrust than the comparable fuel-rich rocket cases (Cases 1, 2 and 5). For example, Cases 2 and 4 use the same amount of air, and they both operate at an overall equivalence ratio of one, but there is a significant difference in their thrust levels. One important difference is that air/fuel combustion occurs at different static pressures in these two cases. In Case 2, the excess fuel from the rocket burns with air in the constant area combustor at a static pressure of ~ 15 psia. On the other hand, in Case 4, the air/fuel combustion occurs in the afterburner at a higher static pressure (~ 17 psia). Heat release at a higher pressure should produce an overall higher efficiency in the cycle. One other factor in the difference in thrust levels of these cases is that the afterburner fuel is hydrogen rather than JP-7. The higher theoretical performance of hydrogen compared to JP-7 has not been taken into account in these observations.

5. GH_2/GO_2 SINGLE AND TWIN ROCKET EJECTOR RESULTS & ANALYSIS

In this chapter, results from a series of RBCC rocket ejector experiments for the Single and Twin B ($\psi = 2.5$ in.) thruster configurations at a thruster chamber pressure of 200 psia are presented and discussed. This test series, which was conducted between May 2000 and May 2001, is referred to as Phase I. A second set of experiments was conducted between September 2002 and May 2003. This second test series is referred to as Phase II. Phase I results are discussed in the current addendum report, whereas Phase II results are discussed in detail in the final report for the contract.

Experiments were conducted at all six of the operating conditions listed in Table 2.9. Raman measurements were made at the Case 3 and Case 6 conditions for the Single thruster configuration and at the Case 6 conditions for the Twin B configuration. The objectives of this test series were to develop a data set for comparing single and twin thruster operating characteristics, and to compare these experimental results with CFD calculations performed by researchers at NASA MSFC [12,13].

Table 5.1 summarizes the types of measurements that were made at each operating condition for the Single thruster. All the results identified in Table 5.1 are archived on the accompanying DVD. Test dates, and in some cases specific test numbers, are identified to simplify the process of accessing data files on the DVD. Table 5.2 provides similar information for the Twin B measurements made during Phase I.

Although data is available for all six test conditions, most of the discussion in this chapter focuses on a comparison of Single and Twin B performance for Case 6. The reader is referred to the DVD for experimental results pertaining to the other cases. This case (i.e., Case 6) was highlighted for two reasons. Unlike the direct-connect cases where the air flow rate is a controlled parameter, during tests at sea-level static (SLS) conditions the primary (thruster) flow induces the secondary (air) flow. As a result, the secondary flow rates for Cases 5 and 6 are a direct measure of the pumping efficiency of the ejector configuration. Additionally, since there is very little excess fuel in the primary stream for Case 6 (MR = 8), this case can be used to study the mixing and pumping phenomena without the effect of significant heat release in the constant area combustor.

Table 5.1. Single thruster data summary table.

Case # ==>	1	2	3	3 - No A/B	4	4 - No A/B	5	6
DATA TYPE								
Heat Flux 2 in. Duct Throat	**Date: 10/30/00** *Test No.: 12,13,28,29* **Date: 11/02/00** *Test No.: 11,12,26,27*	**Date: 10/30/00** *Test No.: 15,16,25,26* **Date: 11/02/00** *Test No.: 15,16,24,25*	**Date: 10/13/00** *Test No.: 9, 11-13, 32* **Date: 10/20/00** *Test No.: 13,21,23,27-30* **Date: 10/23/00** *Test No.: 10,11,19,20-22* **Date: 10/30/00** *Test No.: 9-10* **Date: 10/31/00** *Test No.: 7-9, 11, 14, 15* **Date: 11/02/00** *Test No.: 8, 9, 29, 30*		**Date: 10/30/00** *Test No.: 18,19,22,23* **Date: 11/02/00** *Test No.: 17,18,22,23*		**Date: 11/20/00** *Test No.: 44, 45* **Date: 11/21/00** *Test No.: 15-18* **Date: 11/29/00** *Test No.: 28,30,31* **Date: 11/30/00** *Test No.: 14,17-21*	**Date: 11/20/00** *Test No.: 31-34,36,40* **Date: 11/21/00** *Test No.: 4, 9, 10, 13* **Date: 11/29/00** *Test No.: 7, 11-13, 26* **Date: 11/30/00** *Test No.: 14,17-19,21*
5 in. Duct Throat			**Date: 8/11/00** *Test No.: 8-10, 20, 22-23* **Date: 8/14/00** *Test No.: 8-11, 13, 16-18* **Date: 8/17/00** *Test No.: 7-9, 11-14* **Date: 9/29/00** *Test No.: 7-11* **Date: 10/9/00** *Test No.: 12,18,19,22,26*				**Date: 11/09/00** *Test No.: 27-29* **Date: 11/10/00** *Test No.: 11-12* **Date: 11/13/00** *Test No.: 29-30* **Date: 11/15/00** *Test No.: 24-30*	**Date: 11/09/00** *Test No.: 14-18, 26* **Date: 11/10/00** *Test No.: 8-10* **Date: 11/13/00** *Test No.: 13-16* **Date: 11/15/00** *Test No.: 11-14, 37*
Static Pressure Axial Profiles 2 in. Duct Throat	**Date: 10/30/00** *Test No.: 12,13,28,29* **Date: 11/02/00** *Test No.: 26-27*	**Date: 10/30/00** *Test No.: 15,16,25,26* **Date: 11/02/00** *Test No.: 24-25*	**Date: 10/30/00** *Test No.: 9-10,33-34* **Date: 11/02/00** *Test No.: 29-30*	**Date: 10/30/00** *Test No.: 7-8,30-31*	**Date: 10/30/00** *Test No.: 18,19,22,23* **Date: 11/2/00** *Test No.: 22-23*		**Date: 11/21/00** *Test No.: 15-18*	**Date: 11/20/00** *Test No.: 11-16* **Date: 11/21/00** *Test No.: 7-10* **Date: 12/1/00** *Test No.: 15-18*
Axial Profiles 5 in. Duct Throat	**Date: 7/5/00** *Test No.: 8-10*		**Date: 11/7/00** *Test No.: 24-26*	**Date: 7/5/00** *Test No.: 11-12*		**Date: 7/5/00** *Test No.: 15-17*	**Date: 11/9/00** *Test No.: 27-29* **Date: 11/10/00** *Test No.: 11-13*	**Date: 11/9/00** *Test No.: 10-12* **Date: 11/10/00** *Test No.: 8-10*
Raman 2 in. Duct Throat X = 2.3 in. X = 6.3 in. X = 13.3 in.			**Date: 11/1/00** **Date: 10/20/00**					**Date: 11/20/00** **Date: 11/29-30/00** **Date: 12/1/00**
5 in. Duct Throat X = 2.3 in. X = 6.3 in. X = 9.3 in. X = 13.3 in.			**Date: 9/25/00** **Date: 11/7/00** **Date: 9/29/00**					**Date: 11/15/00** **Date: 11/9/00** **Date: 11/13/00**
Thrust 5 in. Duct Throat							**Date: 11/9/00** *Test No.: 27-29* **Date: 11/10/00** *Test No.: 11-13* **Date: 11/15/00** *Test No.: 24-30*	**Date: 11/9/00** *Test No.: 12-26* **Date: 11/13/00** *Test No.: 11-19,23-28* **Date: 11/15/00** *Test No.: 18-22,33-47*
Air Velocity & **Mass Flow Rate** 2 in. Duct Throat							**Date: 11/21/00** *Test No.: 17-18*	**Date: 11/17/00** *Test No.: 8, 12-14* **Date: 11/20/00** *Test No.: 6-12,14-16* **Date: 11/21/00** *Test No.: 6-9*
5 in. Duct Throat							**Date: 11/15/00** *Test No.: 28-30*	**Date: 11/15/00** *Test No.: 32-37*

Table 5.2. Twin B thruster data summary table.

Case # ==>	1	2	3	4	5	6
DATA TYPE						
Heat Flux	**Date: 1/26/01** *Test No.: 18-20, 36-38, 42-44, 58-60*	**Date: 1/26/01** *Test No.: 22-24, 46-48, 51, 54, 56*	**Date: 5/21/01** *Test No.: 7-11, 21-24* **Date: 5/22/01** *Test No.: 10-13, 28-30, 32-34*	**Date: 5/21/01** *Test No.: 12-15, 17-20* **Date: 5/22/01** *Test No.: 14-16, 18-26*	**Date: 1/29/01** *Test No.: 10-12,16-18, 21-26*	**Date: 5/16/01** *Test No.: 22-26* **Date: 5/17/01** *Test No.: 26-29* **Date: 5/18/01** *Test No.: 9, 10, 20-22*
Static Pressure Axial Profiles	**Date: 1/26/01** *Test No.: 18-20, 30-32, 36-38, 43-44*	**Date: 1/26/01** *Test No.: 22-24, 46-48*	**Date: 5/21/01** *Test No.: 22-24* **Date: 5/22/01** *Test No.: 11-13,28-30, 32-34*	**Date: 5/21/01** *Test No.: 13-15, 18-20* **Date: 5/22/01** *Test No.: 15-18,20-22, 24-26*	**Date: 1/29/01** *Test No.: 13-22*	**Date: 5/16/01** *Test No.: 24-35* **Date: 5/17/01** *Test No.: 23-34* **Date: 5/18/01** *Test No.: 17-35*
Raman X = 1.4 in.						**Date: 5/16/01**
X = 3.4 in.						**Date: 5/17/01**
X = 5.4 in.						**Date: 5/18/01**
X = 6.3 in.						**Date: 1/31/01**
X = 13.3 in.						**Date: 2/2/01**
Thrust	**Date: 1/26/01** *Test No.: 18-20,30-32,36-38, 42-44, 58-60*	**Date: 1/26/01** *Test No.: 22-24, 46-48, 51, 54, 55*	**Date: 5/21/01** *Test No.: 7-11, 22-24*	**Date: 5/21/01** *Test No.: 12-20*	**Date: 1/29/01** *Test No.: 10-18,20-26*	**Date: 5/16/01** *Test No.: 14-32* **Date: 5/17/01** *Test No.: 16-32* **Date: 5/18/01** *Test No.: 14-32*
Air Velocity & Mass Flow Rate					**Date: 1/29/01** *Test No.: 10-15,17, 20-22*	**Date: 5/16/01** *Test No.: 8,9,11-16,18-21* **Date: 5/17/01** *Test No.: 16-28* **Date: 5/18/01** *Test No.: 16-20,22*

5.1. Conventional Measurements

5.1.1. Entrained Air Flow Measurements

The mass flow rate of the secondary stream was derived from a static pressure measurement made on the +Z side wall at the downstream end of the converging inlet section (x = -16.53 in., y = 0.0 in., z = 1.5 in.). The difference between the ambient pressure and the static pressure (p) in the inlet was measured with a differential pressure gage (Setra Systems Inc., Model #239). Assuming the total pressure (P_o) and temperature (T_o) were the ambient values in the laboratory, a one-dimensional velocity of the air stream (V) was calculated using the isentropic compressible flow relationships [14].

$$V = M \cdot a \qquad [5.1]$$

$$M = \sqrt{\left[\left(\frac{P_o}{p}\right)^{\gamma-1/\gamma} - 1\right] \cdot \left(\frac{2}{\gamma - 1}\right)} \qquad [5.2]$$

$$a = \sqrt{\gamma \frac{R_u}{MW} T} \qquad [5.3]$$

$$T = To \cdot \left(1 + \frac{\gamma - 1}{2} M^2\right)^{-1} \qquad [5.4]$$

where,

$M \equiv$ Mach number

$a \equiv$ speed of sound

$\gamma \equiv$ ratio of specific heats (C_p/C_v)

$R_u \equiv$ universal gas constant

$MW \equiv$ molecular weight of the gas

$T \equiv$ static temperature

The mass flow rate was calculated using the relationships [14]:

$$\dot{m} = \rho \cdot A \cdot V \qquad [5.5]$$

$$\rho = \rho_o \Big/ \left(1 + \frac{\gamma - 1}{2} M^2\right)^{1/\gamma - 1} \qquad [5.6]$$

Table 5.3. Entrained air flow rate for SLS tests.

Case	Single Thruster mdot, air (lb_m/s)	Twin B Thruster (Ψ = 2.50 in.) mdot, air (lb_m/s)	Percent Change (%)
Case 5 - *Measured*	**1.02**	**1.13**	10.0
Case 5 - *CFD Prediction*	n/a	n/a	--
Case 5 - *Percent Difference (%)*	--	--	
Case 6 - *Measured*	**1.04**	**1.18**	13.9
Case 6 - *CFD Prediction*	0.84	0.86	2.4
Case 6 - *Percent Difference (%)*	23.3	37.1	

The geometric area of the inlet at the measurement location (A = 15.525 in^2) was used in Equation 5.5. Since the one-dimensional velocity used in equation [5.5] does not account for the velocity profile in the boundary layer, the actual air flow rate will be ~5-10% lower than this calculated value.

Table 5.3 summarizes the entrained air flow rate measurements from the sea-level static (SLS) test cases. Also included in the table are CFD predictions for the entrained air flow rates. These calculations were performed by analysts at NASA/Marshall who modeled the RBCC engine using the FDNS CFD code [12,13]. The CFD air flow rate was calculated by integrating the mass flux across the grid of the secondary flow area at several axial locations. This technique was also used to verify that the continuity equation had been satisfied in the steady-state CFD solution.

There was a significant difference between the Single and Twin B air flow rates (10-14%). This increase in secondary flow for the Twin B is an indication of improved pumping with multiple thrusters. The CFD model, which shows only a 2.4% difference between the two configurations, does not seem to capture the increased air entrainment for the Twin B configuration. In addition, the air flow rates predicted by the CFD model are significantly lower than the corresponding experimental values (23-37%). Several factors may have contributed to this discrepancy in air flow rates. As noted earlier, the calculation of the experimental mass flow rate does not account for the velocity profile in the boundary layer. Also, the experimental air velocity is assumed to be equal to the value of a single point measurement on the duct centerline.

The CFD results may be sensitive to the assumptions made in the FDNS turbulence model. The model used in this study assumed that the turbulence is isotropic. Goebel and Dutton [15] have observed significant anisotropy in their experimental turbulence measurements in a compressible mixing layer. This anisotropy has an effect on the rate of shear layer mixing between a high speed and a low speed gas stream, especially as the flow field becomes more compressible.

5.1.2. Static Pressure Measurements

Figure 5.1 compares axial static pressure profiles for the Single and Twin B configurations at the Case 6 operating conditions. There is little apparent difference between the side and top wall profiles for both cases, except near the thruster exit plane ($x = 0$ in.). The Single and Twin B profiles have similar trends: an initial drop in static pressure below ambient as the air accelerates from the inlet entrance to the thruster exit plane; a sharp rise in pressure in the constant area combustor section ($0 < x < 35.3$ in.), which indicates the extent of primary/secondary mixing; a pressure plateau after mixing is complete; a gradual rise in pressure in the diverging section of the duct ($35.3 < x < 70.2$ in.) indicating that the subsonic mixed flow is slowing down; a slight dip in pressure in the afterburner section ($70.2 < x < 80.2$ in.) due to additional heat release; and, a drop in pressure down to ambient in the converging nozzle section ($80.2 < x < 93.3$ in.).

Despite these similar trends, there are some obvious differences between the Single and Twin B profiles. It should be noted that several static pressure measurement ports were added in

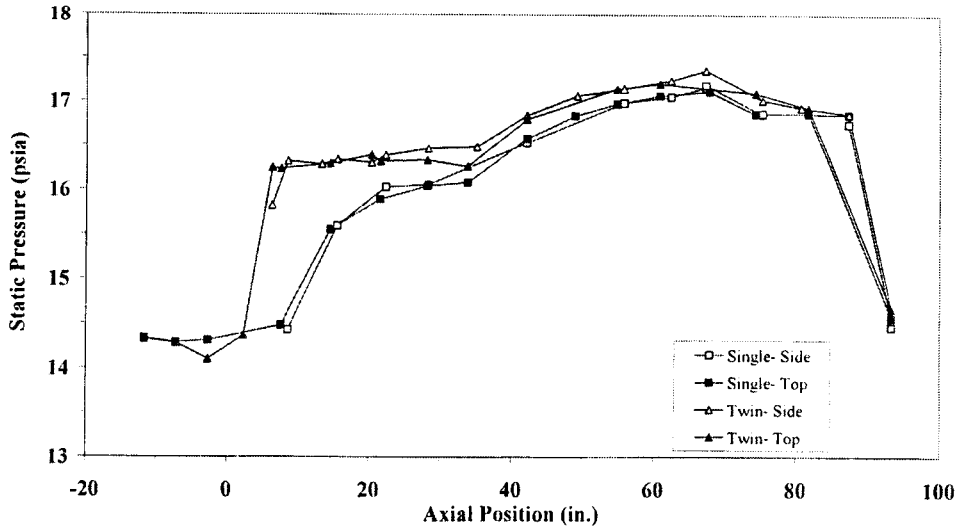

Fig. 5.1. Static pressure axial profiles for Case 6 (both single and twin thrusters).

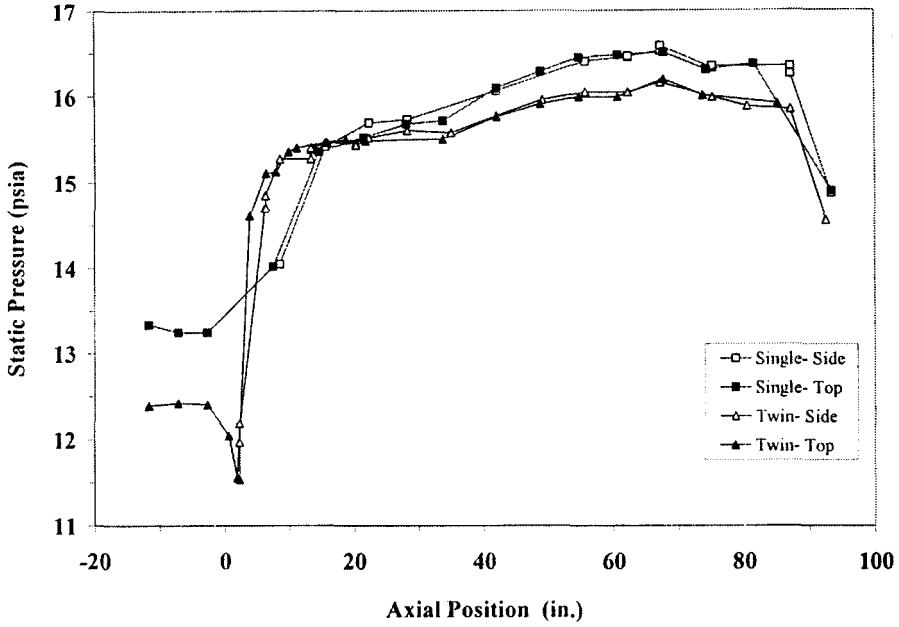

Fig. 5.2. Static pressure axial profiles for Case 3 (both single and twin thrusters).

the mixing region ($0 < x < 20$ in.) for the twin thruster tests. This fact should be considered when comparing the Single and Twin B results in this region. The most obvious difference in the pressure profiles is the location of the sharp rise due to primary/secondary mixing. The Single configuration requires 15-20 inches for complete mixing, but mixing is complete in less than 8 inches for the Twin B configuration. This decrease in mixing length is consistent with the increased shear area of the twin thrusters [3]. The twin thruster also achieves a higher pressure level than the single thruster throughout the length of the duct, which is a result of the higher secondary flow rate in the twin configuration. In absolute terms this difference appears to be small (16.40 versus 16.05 psia in the constant area combustor), but in terms of the pressure rise above ambient (1.70 versus 1.35 psid), this difference is significant (26%).

Figure 5.2 presents the static pressure profiles for the Single and Twin B configurations for the Case 3 conditions. The same general trends are seen in the profiles as in the Case 6 measurements. Once again the Twin B completes mixing much faster than the Single (~ 6 in. versus ~ 15 in.). The fact that no dip in static pressure at $x \sim 0$ is seen in the single thruster profile is probably due to the lack of measurement ports in this region. On the other hand, there is no clear explanation for the difference in the top wall static pressure measurements at $x < 0$ in. for the Single and Twin B configurations. One possible inference is that there is a real difference in the flow field in this region for the two configurations.

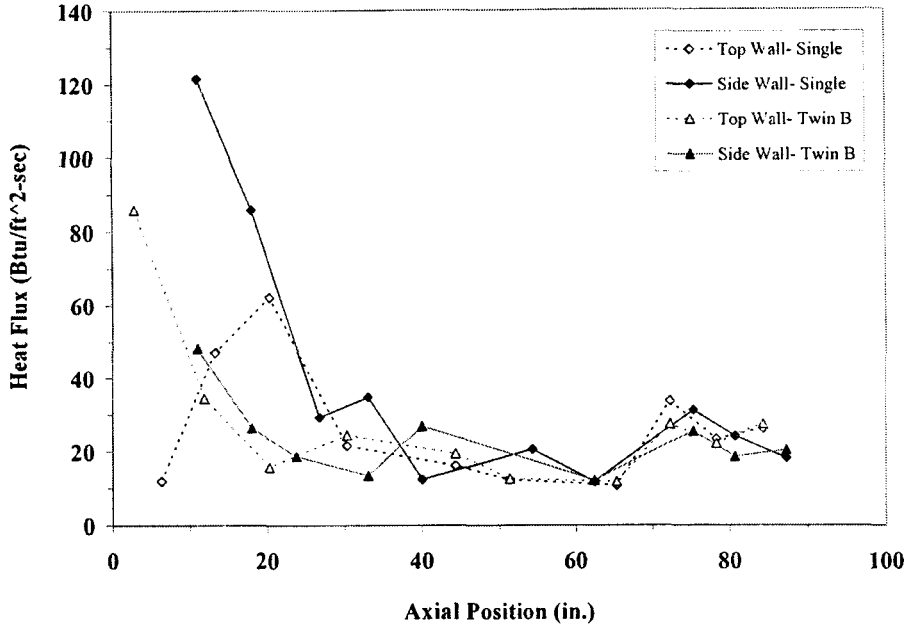

Fig. 5.3. Heat flux comparison between single and twin thruster configurations for Case 6.

5.1.3. Heat Flux Measurements

Figure 5.3 depicts the local heat flux profiles for Case 6. The side wall and top wall measurements are very different in the initial mixing region ($0 < x < 20$ in.) for the single thruster tests. The top wall heat flux measurements are initially much lower than the side wall values. Since the side wall measurements are located on the duct centerline, they are also on the thruster centerline for the single thruster tests. The steep drop in the side wall measurements indicate how rapidly the primary flow stream mixes with the secondary stream. The point where the top wall and side wall measurements converge is another indication that the primary and secondary streams are completely mixed at $x \sim 20$ in.

The Twin B heat flux profiles on the top and side walls are very similar. The side wall measurements are still on the duct centerline, but the thruster centerlines are now at $y = \pm 1.25$ in. Near the thruster exit plane there is a fairly high heat flux at the top wall. This data indicates that the hot primary stream reaches the walls rapidly. Unfortunately, there is no corresponding side wall measurement at this axial location to assess the spreading of the primary streams toward the center of the duct. Further downstream ($x > 30$ in.), all of the Case 6 heat flux profiles have approximately the same values. The rise in heat flux at $x \approx 70$ in. is due to additional combustion in the afterburner.

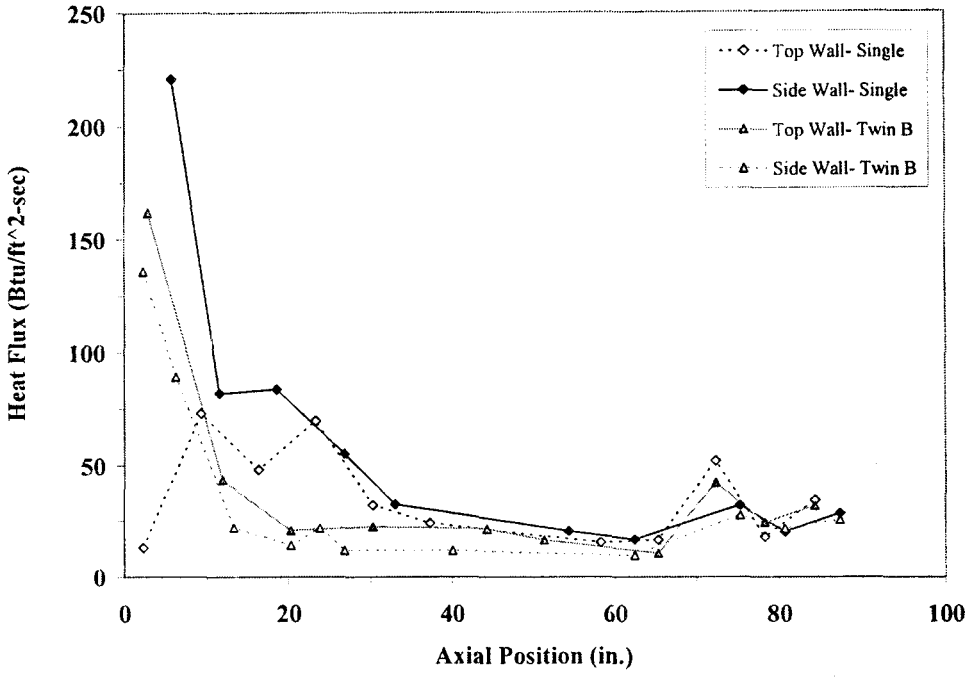

Fig. 5.4. Heat flux comparison between single and twin thruster configurations for Case 3.

Similar trends are seen in the heat flux profiles for Case 3 (Fig. 5.4). For the single thruster configuration, the top and side wall profiles converge at x ~ 10 in. The twin thruster profiles are nearly identical throughout the mixing region.

5.1.4. Thrust Measurements

The thrust measurement results for the Single and Twin B configurations are summarized in Table 5.4. No thrust data was recorded for the Single thruster, direct-connect tests (Cases 1-4) because of problems with the load cell. The differences in thrust for the four Twin B direct-connect cases can be attributed to differences in propellant and/or air flow rates (Table 2.9).

The sea-level static thrust results for the two thruster configurations can be compared directly. For Case 6, the Twin B produces ~ 5% more thrust and entrains ~ 14% more air mass flow rate than the Single configuration. A confidence interval was calculated for this thrust increase (3.4 lb_f) assuming the measurements were normally distributed. The confidence calculations indicate that there is a 95% probability that the Twin B produces at least 2.8 lb_f (4.0%) more thrust than the Single configuration. Since the overall equivalence ratio for Case 6 is less than one, the Twin B thrust increase is due to the entrainment of additional air, not to any additional heat release.

Table 5.4. Summary of thrust measurements for Single and Twin B configurations.

			Single			Twin B			
Operating Condition	O/F Ratio	Simulated Mach Number	Ave. Thrust X_1 (lb_f)	Std. Dev. σ_1 (lb_f)	Total Tests N_1 (N)	Ave. Thrust X_2 (lb_f)	Std. Dev. σ_2 (lb_f)	Total Tests N_2 (N)	Percent Change (%Δ)
Direct Connect									
Case 1	**4**	**1.0**				**31.2**	1.67	15	---
Case 2	**4**	**1.9**				**43.2**	1.38	9	---
Case 3	**8**	**1.0**				**36.5**	1.89	8	---
Case 4	**8**	**1.9**				**52.8**	2.61	8	---
Sea-Level Static									
Case 5	**4**	**0**	**58.9**	1.46	11	**57.1**	1.80	14	**-3.0**
Case 6	**8**	**0**	**69.7**	2.11	47	**73.1**	1.29	48	**4.9**

The Case 5 measurements are more ambiguous. Although the Twin B entrains 10% more air than the Single configuration, Table 5.4 indicates that the Twin B generates less thrust (-3.0%). One issue with the Case 5 thrust data is the small number of samples. Using a t-Student distribution which is valid for small samples, the 95% confidence level is approximately 0.6 lb_f. The thrust decrease from the Single to Twin B configuration is at least 0.6 lb_f (~ 1%). However, this thrust difference is at about the same level as the measurement uncertainties, making it unclear if the decrease is real.

5.2. Raman Major Species Measurements

Raman measurements were made at Case 6 (Single and Twin B) and Case 3 (Single only) operating conditions. While these results provide considerable insight into the details of the flow field, they are based on the average values of Raman signal. Typically, there is considerable frame-to-frame variation in the ICCD images. That unsteady information and its effect on the mixing phenomena are lost in the averaging process.

The transverse position (y) has been normalized by the duct height (h = 5.0 in.) in all of the following Raman profiles. The center of the duct is designated as y/h = 0.0, and the top and bottom walls are at y/h = + 0.5 and y/h = - 0.5, respectively. Also, horizontal dash/dot lines indicate the centerline of each thruster, single or twin, in all of the Raman figures.

5.2.1. Single Thruster Raman Measurements (Case 6, Sea-level Static)

The single thruster temperature profiles derived from the Raman measurements are illustrated in Fig. 5.5. The figure contains results at three axial window locations downstream of the thruster exit plane (x = 2.3, 6.3, and 13.3 in.), as well as the calculated equilibrium temperature [9] for completely mixed primary and secondary flows. The results show that by the first axial location (x = 2.3 in.), the hot primary jet has started to spread symmetrically but the edges of the mixing region have only spread out to approximately y/h = ± 0.12. Since the edges of the rearward facing step of the nozzle are at y/h = ± 0.175, the measurement indicates that the low-temperature secondary flow dominates the recirculation zone caused by the step at x = 0 in. The temperature results near the centerline are very irregular at x = 2.3 in., where the primary flow is the brightest. Typically, Raman measurements have the lowest signal-to-noise ratio in bright flame regions because the number density is low and the background light level is high. By the second window location (x = 6.3 in.) the background light is not a significant factor and the temperature profile is less jagged. The temperature profile at this second location shows the growth of the mixing region. While the center of the jet is relatively flat at the third window (x = 13.3 in.), the temperature decreases smoothly out toward the walls indicating that complete

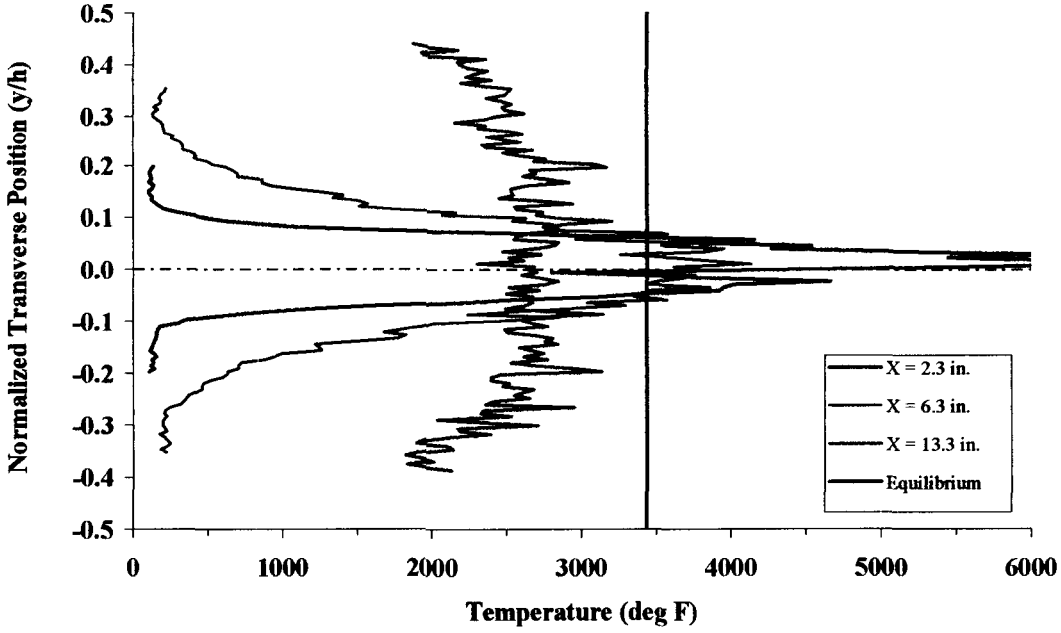

Fig. 5.5. Temperature profiles (Case 6) downstream of single thruster from Raman measurements.

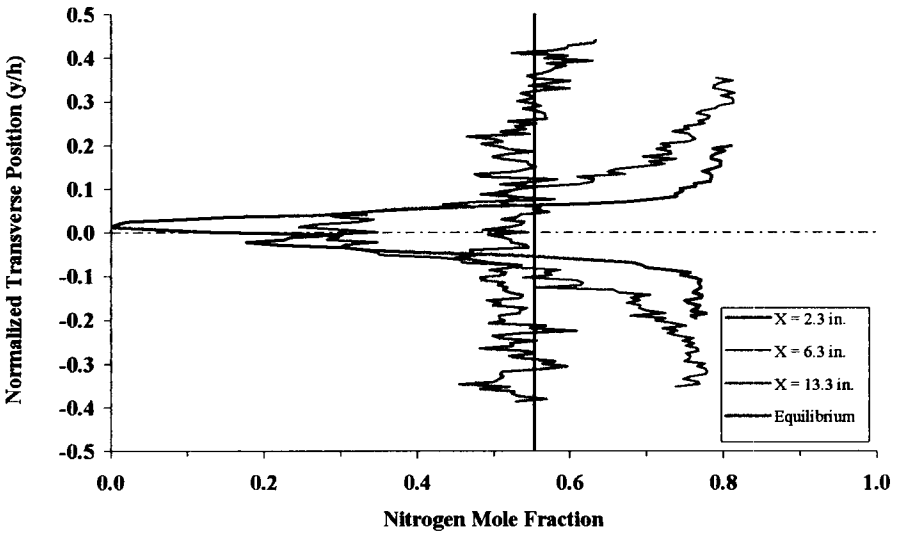

Fig. 5.6. Nitrogen mole fraction profiles (Case 6) downstream of single thruster from Raman measurements.

mixing has not yet occurred. In this and subsequent temperature plots, the measured mixed gas temperature is significantly lower than the equilibrium value. The heat removed from the combustion products by the thruster cooling circuit and the heat transfer through the duct walls has not been accounted for in the equilibrium temperature calculation. These effects would tend to lower the equilibrium temperatures reported here.

Figure 5.6 provides the single thruster nitrogen mole fraction profiles in a format similar to Fig. 5.5. The profile at the first window shows that while the regions away from the centerline are essentially pure air ($XN_2 = 0.79$), very little nitrogen has penetrated into the primary jet region. The other window locations show trends consistent with the temperature results. By the second window, the mixing region has spread, and the flow has approached the equilibrium mole fraction by the third window. Initially, water is only in the hot primary flow stream. Hence, the water mole fraction profiles in Figure 5.7 mimic the trends seen in the temperature data. The oxygen mole fraction profiles (Fig. 5.8) are shaped like those of the nitrogen, though they are noisier and have lower magnitudes. Figure 5.9 shows that near the thruster axis the hydrogen mole fraction is ~ 0.15 - 0.20 at x = 2.3 in. and ~ 0.10 at x = 6.3 in. Equilibrium calculations at the thruster exit plane predict a hydrogen mole fraction of 0.09 for stoichiometric conditions (Case 6). The hydrogen Raman measurements suggest that complete combustion may not be occurring inside the thruster. Finally, an indication that the Raman measurements provide

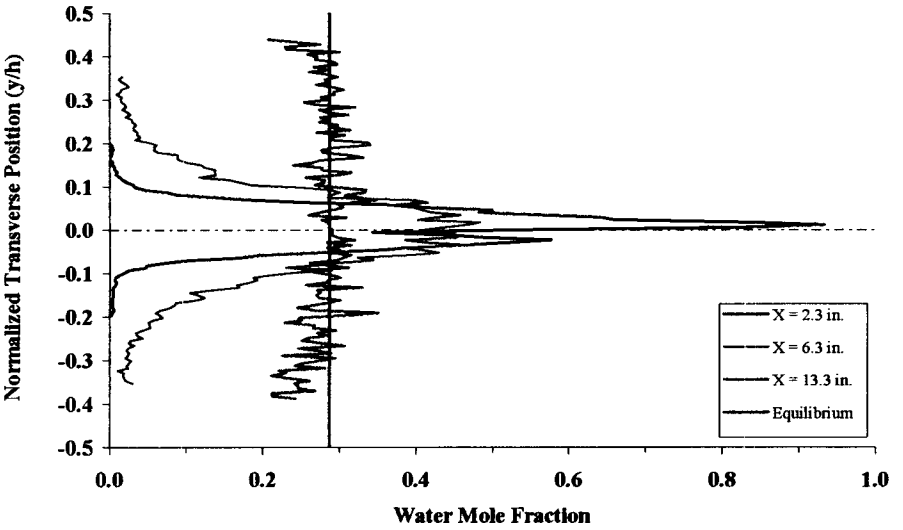

Fig. 5.7. Water mole fraction profiles (Case 6) downstream of single thruster from Raman measurements.

reasonable results is the fact that the mole fraction profiles of the most abundant species, nitrogen and water, are very close to their equilibrium values at x = 13.3 in.

5.2.2. Single Thruster Raman Measurements (Case 3, Direct Connect)

The Case 3 temperature profiles are shown in Fig. 5.10. At the first axial location (x = 2.3 in.), the profile has a shape similar to the corresponding profile for Case 6 (i.e., Fig. 5.5). At the second measurement location (x = 6.3 in.), the flow field is close to being completely

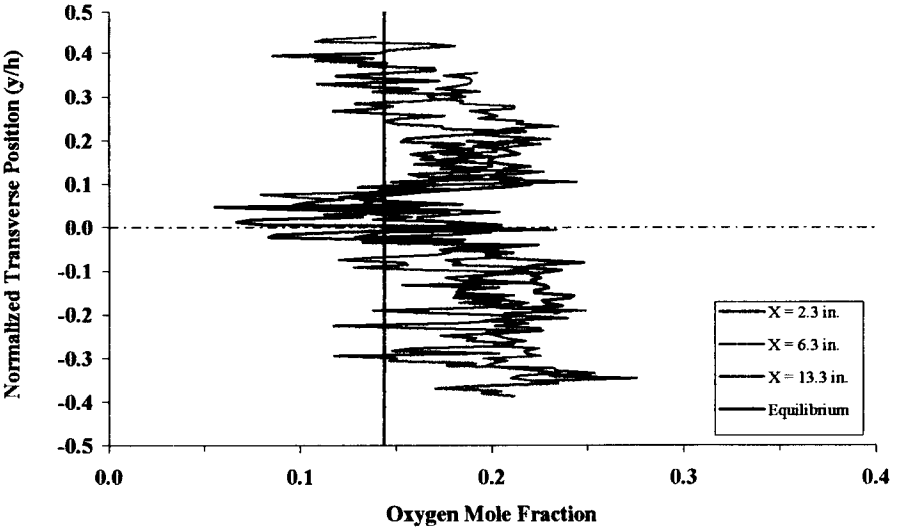

Fig. 5.8. Oxygen mole fraction profiles (Case 6) downstream of single thruster from Raman measurements.

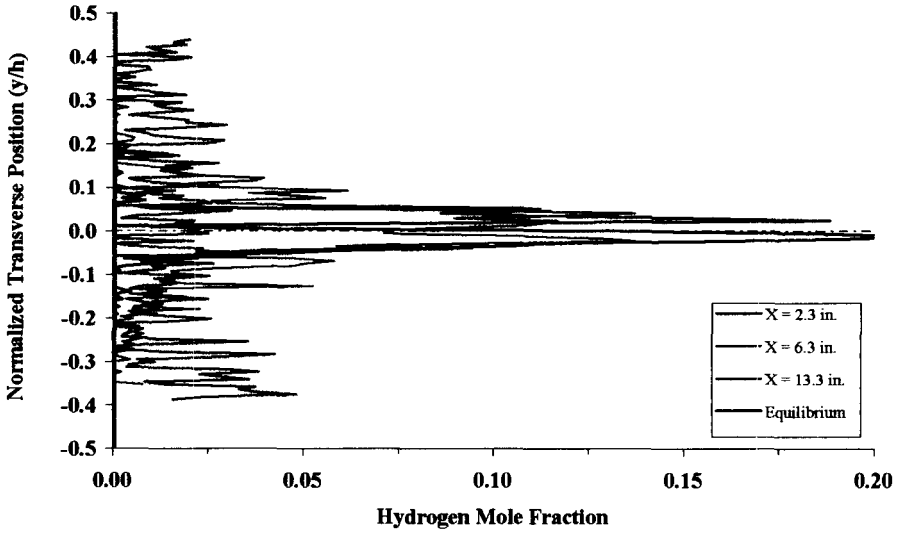

Fig. 5.9. Hydrogen mole fraction profiles (Case 6) downstream of single thruster from Raman measurements.

mixed. The average temperature appears to drop slightly at the third location (x = 9.3 in.). A similar trend is seen in the nitrogen (Fig. 5.11) and water (Fig. 5.12) mole fraction profiles. The mole fractions appear to be slightly closer to their equilibrium values at x = 9.3 in. than they are at x = 6.3 in.

Initially there was no plausible explanation for why the single thruster mixed so much more rapidly for Case 3 than for Case 6. However, through a combination of CFD calculations performed by NASA and some additional tests, it was determined that at the nominal Case 3

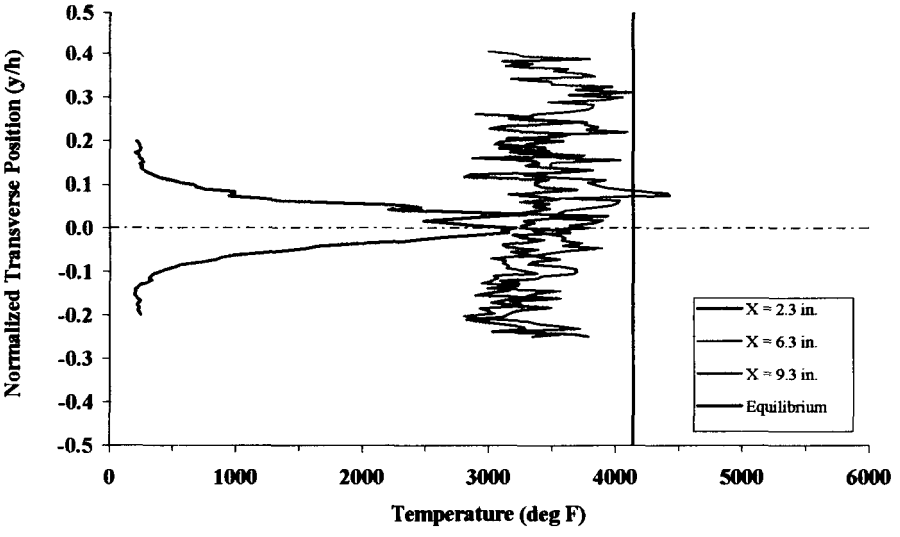

Fig. 5.10. Temperature profiles (Case 3) downstream of single thruster from Raman measurements.

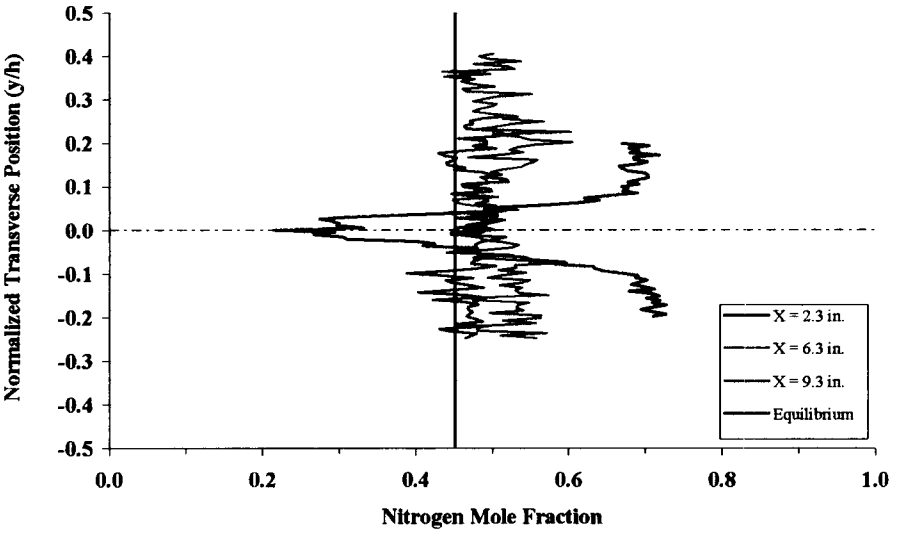

Fig. 5.11. Nitrogen mole fraction profiles (Case 3) downstream of single thruster from Raman measurements.

flow conditions, a large recirculation "bubble" formed in the duct [13]. This bubble severely affected the normal growth of the primary/secondary mixing layer, and it caused very rapid mixing. A series of tests helped determine that the bubble could be eliminated by increasing the nominal Case 3 air flow rate by a factor of ~ 1.6 or greater. Because of the issues associated with the recirculation bubble, no additional Raman measurements were made for any of the Direct Connect cases (Cases 1-4).

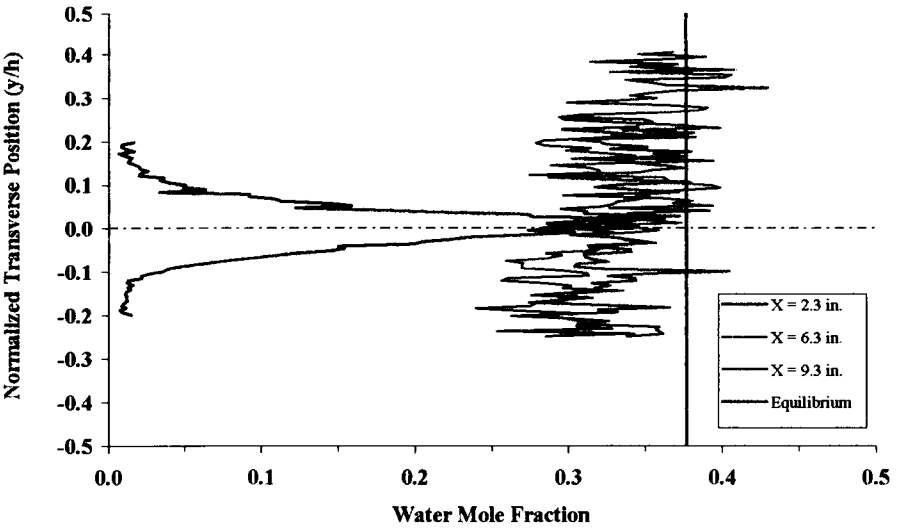

Fig. 5.12. Water mole fraction profiles (Case 3) downstream of single thruster from Raman measurements.

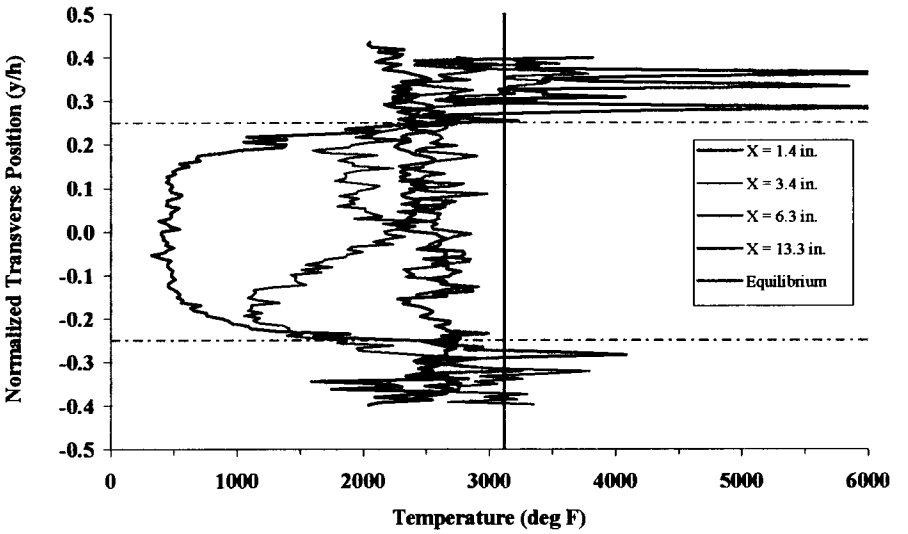

Fig. 5.13. Temperature profiles (Case 6) downstream of twin thrusters from Raman measurements.

5.2.3 Twin Thruster Raman Measurements (Case 6, Sea-level Static, ψ = 2.5 in.)

The Raman temperature profiles for the Twin B configuration are shown in Fig. 5.13. Again, the thruster centerlines (y/h = ± 0.25) are indicated in the figure. Measurements were made at four window locations, but not necessarily the same ones as the single thruster tests. The first temperature profile (x = 1.4 in.) shows that the region between the thrusters is relatively cool (< 500°F) and uniform. The mixing regions are not symmetric about the thruster

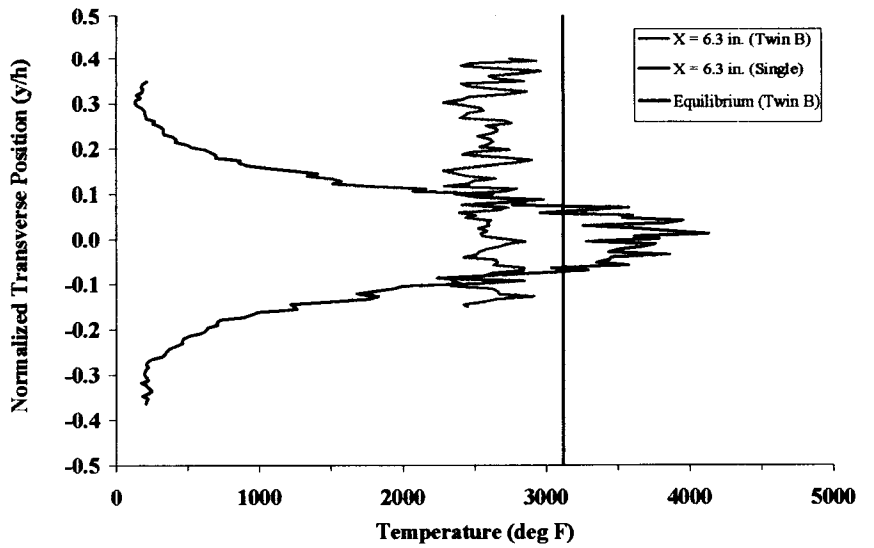

Fig. 5.14. Temperature profile comparison between single and twin thrusters for Case 6 at x = 6.3 in. axial location (from thruster exit plane).

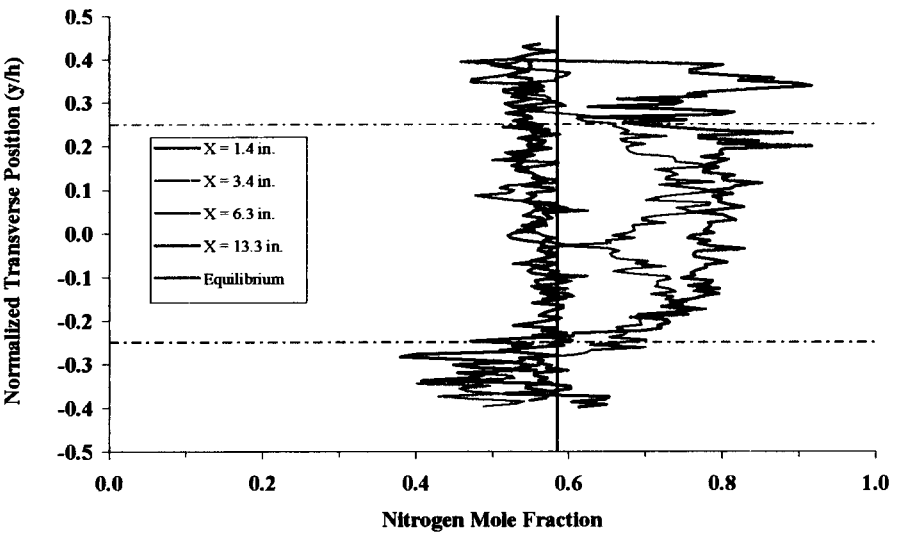

Fig. 5.15. Nitrogen mole fraction profiles (Case 6) downstream of twin thrusters from Raman measurements.

centerlines. The peak temperatures are biased toward the top and bottom duct walls. It also appears that more mixing occurs in the region between the thruster centerlines and the top/bottom walls than in the center of the duct. The second profile (x = 3.4 in.) shows a significant temperature increase in the center region, but it appears that the mixing is still biased toward the walls. The temperature profile at x = 6.3 in. indicates that the mixing is nearly complete, which is consistent with the corresponding static pressure and heat flux measurements. The only difference at x = 13.3 in. may be a slight decrease in the average temperature. Comparing the Single and Twin B temperature profiles at x = 6.3in. (Fig. 5.14) clearly shows the difference between the extent of mixing at that position.

The Twin B nitrogen and water mole fraction profiles are shown in Figs. 5.15 and 5.16, respectively. These mole fraction results are consistent with the single thruster data. High concentrations of nitrogen and low concentrations of water indicate low temperature regions, and vice versa for high temperature regions. The mole fraction profiles are essentially flat and near their equilibrium values at x = 6.3 in. The profiles appear to be slightly closer to equilibrium at x =13.3 in. As with the single thruster results, the mole fraction profiles for the other species were calculated, but they are not presented here.

5.3. Additional Static Pressure Measurements

Because of the noted bias toward the walls in the twin thruster mixing data, experiments were run with additional static pressure taps in the mixing region. Static pressure measurements

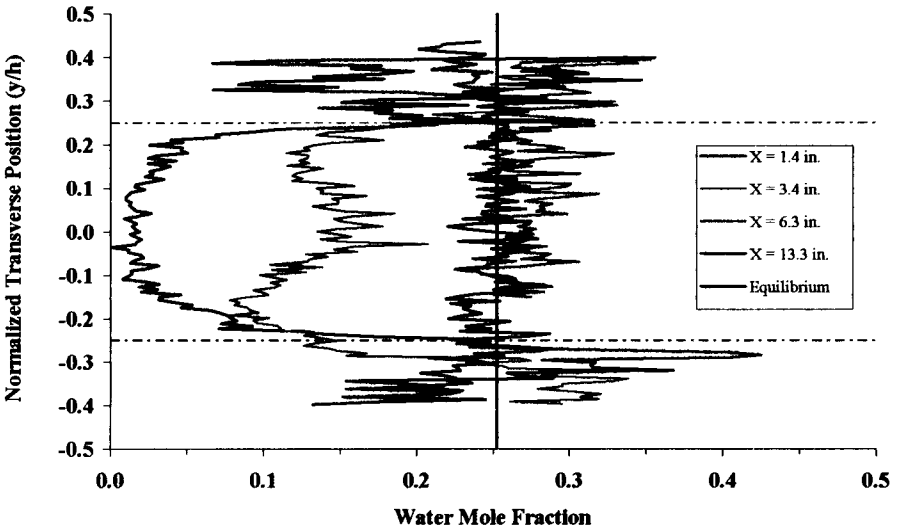

Fig. 5.16. Water mole fraction profiles (Case 6) downstream of twin thrusters from Raman measurements.

were made along the top wall (y = 2.5 in.), along the two thruster centerlines on the side wall (y = ± 1.25 in.), and along the duct centerline on the side wall (y = 0.0 in.). Figure 5.17 summarizes the static pressure results from these experiments. Near the thruster exit plane (x < 8 in.) there was a significant difference in static pressure between the air near the top wall and the air between the thrusters, as much as 2 psid. These pressure measurements indicate that the air moving between the thrusters has a significantly higher velocity than the air between the thruster and the walls. That difference in velocity (and momentum) may explain why the mixing is biased toward the walls.

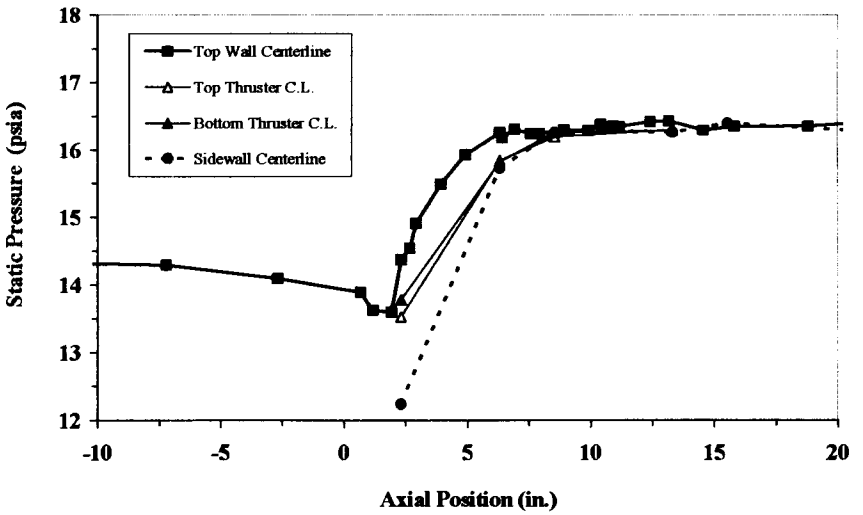

Fig. 5.17. Detailed Static Pressure Map (Case 6, Twin B, Ψ = 2.5 in.).

5.4. Analysis and Interpretation

One of the potential drawbacks of an RBCC system is the low engine thrust-to-weight ratio compared to a rocket engine. The additional weight of the engine offsets some of the performance gains of an RBCC. A key factor in determining the size and weight of an RBCC is the minimum duct length required for efficient mixing and combustion between the rocket exhaust (primary stream) and the entrained air (secondary stream). Therefore, it is important to understand the factors that influence mixing and combustion during the ejector mode of operation.

Two different mixing length analyses were performed and compared to the experimental results. The first analysis (Section 5.4.1) estimates the mixing length using an empirical relationship based on the geometry and operating conditions of the ejector. The second mixing length analysis (Section 5.4.2) is based on results from basic research studies of shear layer growth rates. Although some empiricism is used with this approach as well, the starting point is the fundamental physics of the shear layer mixing process. Finally a boundary layer analysis and a flow stream momentum assessment (Section 5.4.3) were performed to help explain the 'wall bias' phenomenon discussed in Section 5.2.2.

5.4.1. Marquardt Mixing Length Correlation

Based on experimental data from several test programs conducted in the 1960s, the Marquardt Corporation developed an empirical correlation for the optimum mixer length of an ejector ramjet [3, 16-19]. The optimum length, as defined by Marquardt, is the distance from the thruster exit plane to the duct location where the maximum static pressure is attained. In terms of a mixer length-to-hydraulic diameter (D_h) ratio, this correlation is given by:

$$\left.\frac{L}{D_h}\right|_{Optimum} = (0.735 \cdot \Lambda) - 1.0 \qquad [5.7]$$

The correlation parameter (Λ) in equation 5.7 combines a number of geometric and flow parameters in the form:

$$\Lambda = \frac{(A_p/A_s)^{0.33}}{(T_{t,p}/T_{t,s})^{0.15} \cdot N^{0.35}} \left[23.4 + \left(\frac{\dot{m}_s}{\dot{m}_p} \right) M_p^2 \right] \qquad [5.8]$$

Table 5.5. Comparison of predicted and experimental mixing lengths.

		Case 5		Case 6	
		Single	*Twin B*	*Single*	*Twin B*
Area Ratio	A_p/A_s	0.106	0.106	0.106	0.106
Total Temperature Ratio	$T_{T,p}/T_{T,s}$	10.1	10.1	11.5	11.5
Number of Thrusters	N	1	2	1	2
Mass Flow Ratio	m_s/m_p	4.46	4.9	3.88	4.41
Primary Exit Mach Number	M_p	2.45	2.45	2.37	2.37
Correlation Parameter	Λ	16.9	14.0	15.0	12.5
Optimum Length-to-Diameter Ratio	L/D_h	11.4	9.3	10.0	8.2
Predicted Mixing Length	(in.)	42.8	34.8	37.5	30.8
Experimental Mixing Length	**(in.)**	**22** (Mix & Burn)	**8 / 20** (Mix / Burn)	**< 20** (Mix)	**~ 8** (Mix)

This relationship includes the flow area (A_i), total temperature ($T_{t,i}$), mass flow rate ($\dot{m}_i$), and Mach number (M_i) for the primary and secondary flow streams (subscripts "p" and "s", respectively.) Also included in equation 5.8 is the effect of the number of thrusters (N). This relationship ($\Lambda \propto N^{-0.35}$) implies that increasing the number of thrusters will decrease the mixing length. Consequently one of the current research objectives was to perform tests with multiple thrusters to understand the physical effects that may reduce mixing length.

Primary/secondary mixing lengths for the RBCC rocket ejector test article were calculated using the Marquardt empirical correlation given by equations 5.7 and 5.8. The required input parameters come from the duct geometry, measured primary and secondary mass flow rates, and chemical equilibrium calculations for the primary stream exit Mach number and total temperature. Mixing lengths are calculated for the sea-level static conditions (Cases 5 and 6), and the results are compared with mixing lengths estimated from the experimental static pressure profiles. The results of this analysis are summarized in Table 5.5. The experimental mixing lengths are interpreted differently for Cases 5 and 6. For Case 6, where the operating mode is diffusion and afterburning (DAB), the mixing length represents the end of the mixing process between the primary and secondary streams. This point corresponds to the end of the steep rise in the axial pressure profile, as discussed in Section 5.1.2. The Case 5 operating mode is simultaneous mixing and combustion (SMC), and the axial pressure profile has different characteristics. Figure 5.18 shows the axial profile for Twin B operating at Case 5 (MR = 4) conditions. As with the Case 6 profiles there is an initial steep pressure rise at x < 10 in. as the

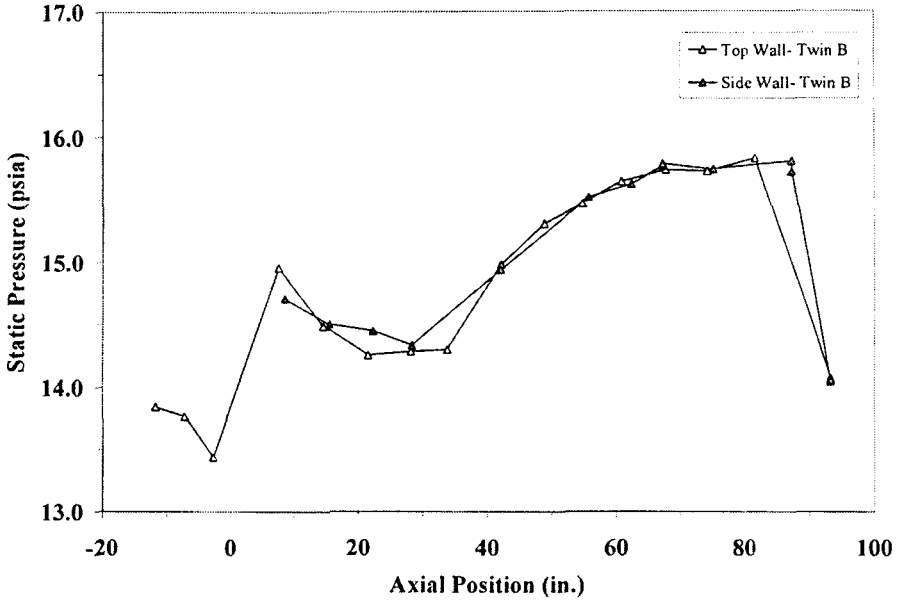

Fig. 5.18. Static pressure axial profile for Twin B configuration, Case 5.

primary and secondary streams mix. Unlike the Case 6 profiles which are basically flat out to the end of the constant area combustor (x = 35.3 in.), the pressure in Fig. 5.18 actually decreases between x = 10 and 20 in. This decrease indicates that hydrogen from the primary flow is still burning and accelerating the bulk flow. There are two distinct steps in this case- the primary and secondary streams mix completely at a macro-scale (x < 10 in.), followed by micro-scale mixing and combustion. Two mixing lengths appear in Table 5.5 for Case 5/Twin B, one indicating the end of the bulk mixing, and the other one indicating the end of the combustion process. The Case 5/Single rocket pressure profile does not have the hump seen in Figure 5.18. Instead there is a gradual pressure rise until a plateau is reached at x ~ 22 in. This gradual pressure rise indicates that the mixing (pressure increase) and combustion (pressure decrease) occurs simultaneously.

It is clear from Table 5.5 that the Marquardt predictions overestimate the actual mixing lengths by a factor of two or more. It is also clear that the Marquardt correlation does not properly capture the trend in mixing length due to the number of thrusters ($N^{-0.35}$). The correlation predicts a decrease in mixing length of approximately 18% when the number of thrusters is doubled. The test results show that the twin thruster mixing lengths are at least 50% shorter than the single thruster values.

One of the drawbacks of the Marquardt mixing length analysis is the empirical nature of correlating data from several different test articles with different numbers of thrusters ($N = 1, 4, 8, 36$). It is difficult to determine the real physical effects due to the number and configuration of the thrusters from equations 5.7 and 5.8.

5.4.2. Mixing Layer Spreading Rate Analysis

A significant amount of experimental research has been performed to develop an understanding of compressible shear layer mixing phenomena [20-25]. Most of these experiments have used ambient temperature, non-reacting gases. As a result, the experimental range of the characteristics flow parameters, specifically the secondary/primary velocity ratio ($r \equiv U_2/U_1$) and density ratio ($s \equiv \rho_2/\rho_1$), has been fairly narrow. Typically in these studies, the velocity ratio is greater than 0.1, and the density ratio is between 0.1 and 10. Combusting flow fields, like the RBCC ejector, often operate well outside of this range. Table 5.6 summarizes these parameters, as well as other flow parameters, for the RBCC experiments. In all of the experimental cases, the velocity ratio is ~0.02 and the density ratio is ~20.

Using the velocity and density ratios, Dimotakis [24] developed the following relationship for the growth rate of an incompressible shear layer (δ'_o):

$$\delta'_o \equiv \frac{\delta_o}{x} = C_\delta \cdot \left[\frac{(1-r)(1+\sqrt{s})}{2(1+r\sqrt{s})}\right] \cdot \left\{1 - \frac{(1-\sqrt{s})/(1+\sqrt{s})}{1+2.9(1+r)/(1-r)}\right\} \qquad [5.9]$$

Empiricism enters equation 5.9 in the experimentally-determined coefficient (C_δ). The constant in the denominator of the last term (i.e., 2.9) also depends on the empirical value of the vortex spacing growth rate (l/x ~0.17) [26]. Shear layer growth rates studies have been extended to compressible flow situations by several researchers [27-32]. Results from these various studies were compiled and analyzed by Slessor [23]. The compressible shear layer growth rates (δ') were normalized by the incompressible values given by equation 5.9 (δ'/δ'_o). Using the energy equation for compressible flow, Slessor developed a compressibility parameter (Π_c) of the form:

$$\Pi_c = \max_i \left[\sqrt{\frac{\gamma_1 - 1}{a_1}}(U_1 - U_2) \;,\; \sqrt{\frac{\gamma_2 - 1}{a_2}}(U_1 - U_2)\right] \qquad [5.10]$$

Using this compressibility parameter, Slessor was able to collapse the various normalized shear layer growth rate data sets to a single curve as shown in Fig. 5.19.

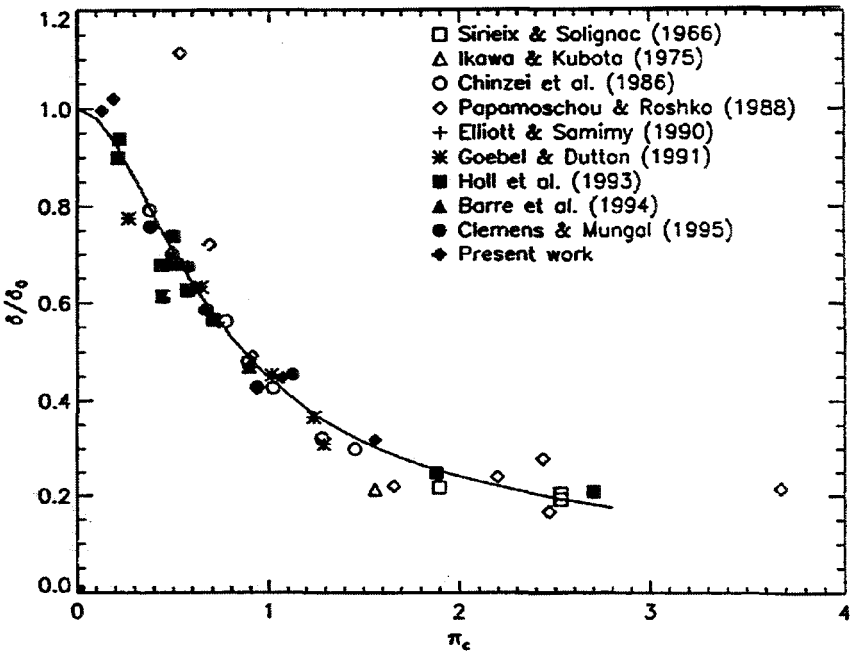

Fig. 5.19. Normalized shear layer growth rate versus Π_c (from Slessor [23]).

The flow parameters in Table 5.6 are used to estimate the shear layer growth rate based on Slessor's compressibility parameter (Π_c). Table 5.7 provides a summary of the shear layer growth rate analysis. The values of Π_c for the RBCC experiments are much larger than any of the values reported by Slessor (Figure 5.19) [23]. It is assumed that the normalized shear layer growth rate (δ'/δ'_o) remains constant at 0.2 for these highly compressible flows ($\Pi_c > 3$). The resulting predictions of compressible growth rate (δ') are all approximately 0.1.

The experimental growth rates are derived from the Raman temperature profiles. Since the initial thruster jet height (0.33 in.) is thin compared to the duct height (5.0 in.), growth of the mixing layer from the edge of the nozzle into the primary stream is assumed to be negligible. Only the mixing layer growth into the secondary stream is considered. The outer boundary of the mixing layer is defined as the point where the temperature profile increased a specified amount above the secondary free stream value. This specified temperature rise is 1% of the temperature difference between the two free streams [$\Delta T = 0.01 \cdot (T_1 - T_2)$]. The mixing layer growth rate can only be determined for the single thruster at Case 6 conditions. Because of the biasing of the primary flows toward the outer walls, it is not possible to establish the growth rates for the Case 6, Twin B data.

Table 5.6. Characteristic flow parameters for the RBCC rocket ejector test article.

			Case 5		Case 6	
			Single	*Twin B*	*Single*	*Twin B*
Primary Velocity	U_1	ft/s	11340	11340	9680	9680
Secondary Velocity	U_2	ft/s	203	223	205	233
Velocity Ratio	r	(U_2/U_1)	0.018	0.020	0.021	0.024
Primary Mach Number	M_1	(U_1/a_1)	2.45	2.45	2.37	2.37
Secondary Mach Number	M_2	(U_2/a_2)	0.18	0.20	0.18	0.21
Primary Density	ρ_1	lb_m/ft^3	3.00E-03	3.00E-03	4.10E-03	4.10E-03
Secondary Density	ρ_2	lb_m/ft^3	7.63E-02	7.63E-02	7.63E-02	7.63E-02
Density Ratio	s	(ρ_2/ρ_1)	25.4	25.4	18.6	18.6
Momentum Ratio	λ_{Mo}	$(\rho_2U_2^2/\rho_1U_1^2)$	8.15E-03	9.84E-03	8.35E-03	1.08E-02
Primary Flow Rate	$mdot_1$	lb_m/s	0.235	0.235	0.273	0.273
Secondary Flow Rate	$mdot_2$	lb_m/s	1.05	1.15	1.06	1.21
Mass Flow Ratio	λ_m	$(mdot_2/mdot_1)$	4.46	4.90	3.88	4.42

The results for the single thruster indicate that the experimental mixing layer growth rate (measured δ') is approximately twice the value predicted by Slessor's compressible shear layer (theoretical δ') correlation (~0.2 versus ~0.09). Some of the factors that could have contributed to this higher growth rate include heat release in the mixing region [33, 34], an adverse pressure gradient [20, 36], and three-dimensional effects [37]. The most likely cause of the increased shear layer growth rate is the adverse pressure gradient. Because of the presence of significant amounts of hydrogen in the primary flow (Fig. 5.9), heat release in the mixing layer may have been a contributing factor.

Despite the difference between the predicted and measured values of δ', the shear layer growth theory provides a much better estimate of the RBCC mixing length than the Marquardt correlation. In addition, the shear layer approach seems to capture the effect of changing the number of thrusters on mixing length, at least for a change from one to two thrusters.

5.4.3. Analysis of the Wall Bias in the Twin B Mixing Layers

The Twin B Raman results in Figs. 5.13, 5.15, and 5.16 indicate a strong asymmetry in the mixing process. As seen in the temperature plot (Fig. 5.13), the primary flow streams are

Table 5.7. Summary of shear layer growth parameters for the RBCC rocket ejector test article.

			Case 5		Case 6	
			Single	*Twin B*	*Single*	*Twin B*
Total Convective Mach Number	Mc	$[\Delta U/(a_1 + a_2)]$	1.94	1.93	1.82	1.82
Compressibility Parameter	Π_c	(Slessor)	6.30	6.29	5.36	5.34
Growth Rate Scaling Factor	C_δ	(Slessor)	0.17	0.17	0.17	0.17
Incompressible Growth Rate	δ_o'	(Equation 5.9)	0.540	0.535	0.469	0.462
Normalized Growth Rate	δ'/δ_o'	(assumed)	0.2	0.2	0.2	0.2
Compressible Growth Rate	$\delta'_{,\,theo}$	--	0.108	0.107	0.094	0.092
Measured Growth Rate	$\delta'_{,\,act}$	--	n/a	n/a	0.203	??
Predicted Mixing Length	$L_{mix,\,theo}$	(in)	23.1	11.7	26	13.3
Measured Mixing Length	$L_{mix,\,act}$	**(in)**	**22** (Mix & Burn)	**8 / 20** (Mix / Burn)	**< 20** (Mix)	**~ 8** (Mix)

pushed off of their centerlines toward the top or bottom wall. This biasing of the primary flow indicates that the secondary flow in the center region ($A_{2,c}$) has a higher momentum than the secondary flow near the walls ($A_{2,w}$).

The static pressure measurements in the two secondary regions, $A_{2,c}$ and $A_{2,w}$, are used to analyze the flow characteristics in those regions. Table 5.8 summarizes the results of this analysis. By assuming isentropic, compressible flow, the static pressure readings at x = 2.3 in. are used to estimate the Mach number, velocity, and density of the air streams in the center ($A_{2,c}$) and near-wall ($A_{2,w}$) regions. Ideally, static pressure measurements at x = 0.0 in. would have been used for these calculations, but measurements are not available at that axial location. Based on the static pressure measurements, the Mach number in the two secondary regions differs by a factor of 3 (0.52 versus 0.18). The resulting split in the secondary mass flow rate (72%/28%) is quite different than a nominal 50%/50% split based simply on the geometric flow areas.

This analysis overestimates the total secondary mass flow rate by ~45%. The calculated mass flow rates are then modified by correcting the flow areas to account for boundary layer growth. Since some of the boundary layers in this region begin to develop at the RBCC duct inlet and others begin at the front of the thrusters, the flow areas are not affected uniformly (Fig. 5.20). Flat plate boundary layer theory [38] is used to estimate the thickness of the boundary layers (δ) on each bounding surface at the thruster exit plane:

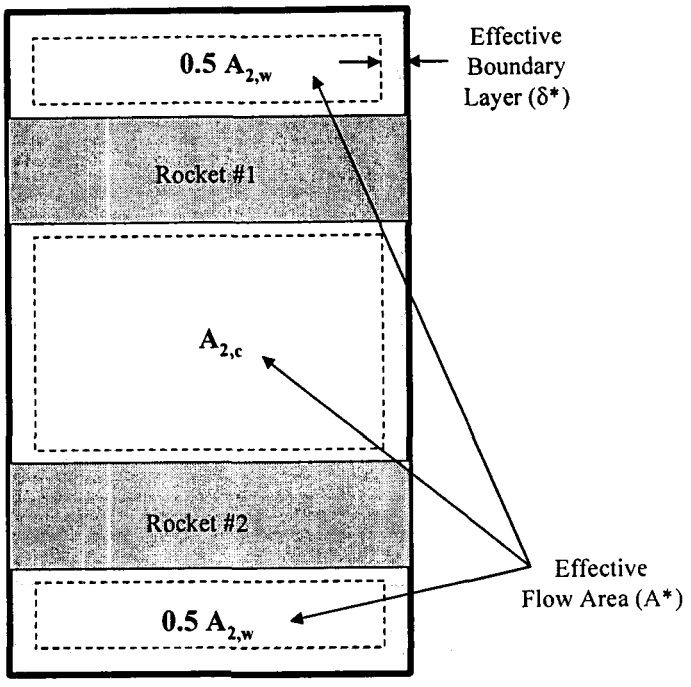

Duct End View

Fig. 5.20. Boundary layer growth in the secondary flow passages.

$$\left.\frac{\delta}{x}\right|_{lam} = \frac{5.0}{(\mathrm{Re}_x)^{1/2}} \qquad \text{or} \qquad \left.\frac{\delta}{x}\right|_{turb} = \frac{0.16}{(\mathrm{Re}_x)^{1/7}}$$

where the Reynolds number (Re_x) is based on the axial distance along the plate (x). That distance at the thruster exit plane is ~26 in. for flow along the top, bottom and side walls of the duct, and ~ 12 in. for flow over the thruster bodies. The laminar-to-turbulent transition occurs at $\mathrm{Re}_x \sim 10^6$. The displacement thickness (δ^*) is defined as the thickness of an equivalent boundary layer which allows no flow to pass through it. This displacement thickness is given by:

$$\delta^*_{lam} \approx \frac{\delta}{3} \qquad \text{or} \qquad \delta^*_{turb} \approx \frac{\delta}{8}$$

These displacement thicknesses are used to estimate the effective flow areas, $A^*_{2,c}$ and $A^*_{2,w}$, shown in Table 5.8. The corrected total mass flow rate is still greater than the actual value by ~33%. Despite this difference in the secondary mass flow rate, momentum ratios between the primary flow stream and the two secondary flow streams are calculated. The momentum ratios

Table 5.8. Secondary air flow characteristics for the Twin B configuration (Ψ = 2.5 in.).

			Total or Stagnation Value	Center Region Value	Wall Region Value
Flow Area	$A_{2,i}$	(sq in)	9.75	4.875	4.875
Pressure		(psia)	14.70	12.24	14.37
Mach Number				0.518	0.178
Density		(lb_m/ft^3)	0.0749	0.0657	0.0737
Temperature		(deg R)	530	503	527
Acoustic Velocity		(ft/s)	1129	1100	1125
Velocity		(ft/s)	--	569	201
Mass Flow Rate		(lb_m/s)	1.77	1.27	0.50
Flow Split		(%)	100	71.7	28.3
B.L. Area Correction			--	0.924	0.853
Corrected Area	$A^*_{2,i}$	(sq in)	8.66	4.50	4.16
Corrected Mass Flow		(lb_m/s)	1.60	1.17	0.43
Corrected Flow Split		(%)	100	73.3	26.7
Momentum Ratio	$(\rho_2 U_2^2/\rho_1 U_1^2)$		--	5.54E-02	7.71E-03

for the center and wall regions differ by a factor of ~7, confirming that the secondary flow in $A_{2,c}$ has a much higher momentum than the flow in $A_{2,w}$.

6. SUMMARY

A series of studies conducted to investigate the operation of rocket ejector systems applicable to Rocket-Based Combined Cycle (RBCC) engines has been completed. These studies investigated a range of flow conditions to examine the effect of rocket chamber pressure, by-pass ratio and rocket stoichiometry on ejector performance in terms of mixing and thrust. Both single rocket and twin rocket configurations were studied to examine the effect of increasing the number of rockets.

Measurements of the pressure profile along the ejector duct, the heat flux to the duct wall and the species concentration field downstream of the rocket were determined. Both direct connect and sea level static inlet conditions were investigated. Single and twin rocket studies for gaseous hydrogen/oxygen propellants and single rocket studies for the JP-7/gaseous oxygen propellants were conducted. Thrust measurements were obtained for all the operating conditions. For the gaseous hydrogen/oxygen single and twin rocket cases, measurements of the mixing length determined from pressure profiles and species concentration fields were used to assess differences in the ejector performance.

Concurrent Computational Fluid Dynamic (CFD) modeling done by researchers at the Marshall Space Flight Center was used to validate the CFD models as well as to help guide the experiments. All of the data obtained have also been placed on a DVD disc for future availability.

Some of the major results of the study include the following:

- The mixing lengths of single and twin rocket studies were found to be reasonably well predicted for a mixing layer model developed from existing theories on shear layer mixing.
- The twin rocket ejector studies indicated significantly shorter mixing length than the single rocket case for conditions where the blockage ratio, nozzle exit area and rocket propellant flows were the same. This result has important implications in terms of the mixing section length for practical RBCC engines.

Finally, an extensive data base for rocket ejector analysis has been obtained that can assist in CFD model development. The extensive nature of this data is remarkable and will serve as a valuable resource for future RBCC engine development.

7. REFERENCES

[1] Escher, W. J. D., ed., *The Synerjet Engine: Airbreathing/Rocket Combined-Cycle Propulsion for Tomorrow's Space Transports*, PT-54, Progress in Technology Series, Society of Automotive Engineers, Warrendale, PA, 1997.

[2] Santoro, R. J. and Pal, S., Experimental and Analytical Modeling of the Rocket Ejector Mode of a Combined Cycle Rocket-Based Engine, Final Report Submitted to NASA MSFC for NASA Contract Grant NAS8-40890, June 2001.

[3] Odegaard, E. A. and Stroup, K. E., "1966 Advanced Ramjet Concepts Program, Volume VIII- Ejector Ramjet Engine Tests- Phase I," The Marquardt Corporation, Technical Report AFAPL-TR-67-118 Volume VIII, January 1968.

[4] Billig, F. S., Advanced Propulsion Technology Program, SSTO Low Speed System Assessment Final Report, The Johns Hopkins University Applied Physics Laboratory, JHU/APL AL-95-A050, 1995.

[5] Lehman, M. K., "Mixing and Reaction Processes in Rocket Based Combined Cycle and Conventional Rocket Engines," Ph.D. Thesis, The Pennsylvania State University, August 2000.

[6] Lehman, M., Pal, S., Schwer, D., Chen, J. D. and Santoro, R. J., "Focused Experimental and Analytical Studies of the RBCC Rocket-Ejector Mode," 36th JANNAF Combustion Subcommittee Meeting, Cocoa Beach, FL, October 18-21, 1999.

[7] Lehman, M., Pal, S. and Santoro R. J., "Experimental Investigation of the RBCC Rocket-Ejector Mode," AIAA Paper 2000-3725, 36th Joint Propulsion Conference, Huntsville, AL, July 2000.

[8] Burkardt, L. A. and Franciscus, L. C., RAMSCRAM--A Flexible Ramjet/Scramjet Engine Simulation Program, NASA Technical Memorandum 102451, 1990.

[9] McBride, B. J. and Gordon, S., Computer Program for Calculation of Complex Chemical Equilibrium Compositions and Applications, NASA Reference Publication 1311, June 1996.

[10] Eckbreth, A. C., *Laser Diagnostics for Combustion Temperature and Species*, Eds. A. K. Gupta and D. G. Lilley, Volume 7, *Energy and Engineering Science Series*, Abacus Press, Cambridge, MA, 1988.

[11] Foust, M. J., Pal, S. and Santoro, R. J., "Gaseous Propellant Rocket Studies Using Raman Spectroscopy," AIAA Paper 96-2766, July 1996.

[12] Ruf, J. H., "Benchmark of FDNS CFD Code for Direct Connect RBCC Test Data," AIAA Paper 2000-3726, July 2000.

[13] West, J., Ruf, J. H., Cramer, J., Pal, S. and Santoro, R. J., "Computational Insight to an Experimentally Observed Change in the Mixing Characteristics of an RBCC Engine in Ejector Mode," AIAA Paper 2001-3459, July 2001.

[14] Zucrow, M. J. and Hoffman, J. D., *Gas Dynamics, Vol. 1*, 1st Ed., John Wiley & Sons, New York, 1976, pp. 172-174.

[15] Goebel, S. G. and Dutton, J. C., "An Experimental Investigation of Compressible, Turbulent Mixing Layers," TR UILU ENG 90-4005, Dept. of Mechanical and Industrial Engineering, Univ. of Illinois at Urbana-Champaign, Urbana, IL, 1990.

[16] Stroup, K. E. and Atkins, T. G., "Supercharged Ejector Ramjet Subscale Feasibility Test Program- Final Report," Marquardt Report 20,436, September 1968.

[17] Totten, J. K. and Campbell, J. R., "Final Summary Technical Report on the Calendar Year 1963 Ramjet Technology Program, Volume 2, Jet Compressors and Ejector Ramjet Investigations," Marquardt Report 25,116, April 1964.

[18] Stroup, K. E. and Pontzer, R., "1966 Advanced Ramjet Concepts, Volume I- Ejector Ramjet Systems Demonstration," The Marquardt Corporation, Technical Report AFAPL-TR-67-118, June 1968.

[19] Flornes, B. J. and Stroup, K. E., "1964 Advanced Ramjet Concepts Program, Volume I- Advanced Jet Compression Engine Concepts," The Marquardt Corporation, Technical Report AFAPL-TR-65-32, May 1965.

[20] Dimotakis, P. E., "Turbulent Free Shear Layer Mixing and Combustion," *High-Speed Flight Propulsion Systems*, edited by S. N. B. Murthy and E. T. Curran, Vol. 137, Progress in Astronautics and Aeronautics, AIAA, New York, 1991, pp. 265-340.

[21] Papamoschou, D. and Roshko, A., "The compressible turbulent shear layer: an experimental study," *Journal of Fluid Mechanics*, Vol. 197, 1988, pp. 453-477.

[22] Hall, J. L., Dimotakis, P. E. and Rosemann, H., "Experiments in Nonreacting Compressible Shear Layers," *AIAA Journal*, Vol. 31, No. 12, Dec. 1993, pp. 2247-2254.

[23] Slessor, M. D., "Aspects of Turbulent-Shear-Layer Dynamics and Mixing," Ph.D. Thesis, California Institute of Technology, 1998.

[24] Dimotakis, P. E., "Two-Dimensional Shear Layer Entrainment," *AIAA Journal*, Vol. 24, No. 11, Nov. 1986, 1791-1796.

[25] Papamoschou, D., "Structure of the Compressible Turbulent Shear Layer, *AIAA Journal*, Vol. 29, No. 5, May 1991, pp. 680-681.

[26] Brown, G. L. and Roshko, A., "On density effects and large structure in turbulent mixing layers," *Journal of Fluid Mechanics*, Vol. 64, Part 4, 1974, pp. 775-816.

[27] Goebel, S. G. and Dutton, J. C., "Experimental Study of Compressible Turbulent Mixing Layers," *AIAA Journal*, Vol. 29, No. 4, April 1991, pp. 538-546.

[28] Chinzei, N., Masuya, G., Komuro, T., Murakami, A. and Kudou, K., "Spreading of two-stream supersonic turbulent mixing layers," *Physics of Fluids*, Vol. 29, No. 5, May 1986, pp. 1345-1347.

[29] Barre, S., Quine, C. and Dussauge, J. P., "Compressibility effects on the structure of supersonic mixing layers: experimental results," *Journal of Fluid Mechanics*, Vol 259, 1994, pp. 47-78.

[30] Sirieix, M. and Solignac, J. L., "Contribution a l'etude experimentale de la couche de mélange turbulent isobare d'un ecoulment supersonique," AGARD Conference Proceedings No. 4, Separated Flows, 1966.

[31] Ikawa, H. and Kubota, T., "Investigation of Supersonic Turbulent Mixing Layer with zero pressure gradient," *AIAA Journal*, Vol. 13, 1975, pp. 566-572.

[32] Samimy, M. and Elliott, G. S., "Effects of Compressibility on the Characteristics of Free Shear Layers," *AIAA Journal*, Vol. 28, No. 3, pp. 439-445.

[33] Keller, J. O. and Daily, J. W., "The Effects of Highly Exothermic Chemical Reaction on a Two-Dimensional Mixing Layer," *AIAA Journal*, Vol. 23, No. 12, Dec. 1985, pp. 1937-1945.

[34] Hermanson, J. C. and Dimotakis, P. E., "Effects of heat release in a turbulent, reacting shear layer," *Journal of Fluid Mechanics*, Vol. 199, 1989, pp. 333-375.

[36] Sabin, C. M., "An Analytical and Experimental Study of the Plane, Incompressible, Turbulent Free-Shear Layer with Arbitrary Velocity Ratio and Pressure Gradient," *Transactions of the ASME, Series D*, Vol. 87, June 1965, pp. 421-428.

[37] Clemens, N. T. and Mungal, M. G., "Large-scale structure and entrainment in the supersonic mixing layer, *Journal of Fluid Mechanics*, Vol. 284, 1995, pp. 171-216.

[38] Schlichting, H., *Boundary-Layer Theory*, trans. J. Kestin, 7th Edition, McGraw-Hill, New York, 1979.

8. PUBLISHED PAPERS

[1] Ruf, J., Lehman, M., Pal, S., Santoro, R. J. and West, J., "Experimental/Analytical Characterization of the RBCC Rocket-Ejector Mode," 37th JANNAF Combustion Subcommittee Meeting, Monterey, CA, October 18-21, 2000.

[2] Santoro, R. J., Pal, S., Woodward, R. D. and Schaaf, L., "Rocket Testing at University Facilities," AIAA-2001-0748, 39th AIAA Aerospace Sciences Meeting and Exhibit, Reno, NV, January 8-11, 2001.

[3] Cramer, J. M., Greene, M., Pal, S. and Santoro, R. J., "RBCC Ejector Mode Operating Characteristics for Single and Twin Thruster Configurations," AIAA-2001-3464, 37th AIAA/ASME/SAE/ASEE Joint Propulsion Conference, Salt Lake City, UT, July 8-11, 2001.

9. MEETINGS

[1] Cramer, J., Lehman, M., Pal, S., Lee, S. Y. and Santoro, R. J., "Status Report on the Penn State RBCC Test Program," Propulsion Engineering Research Center, Penn State, Twelfth Annual Symposium, The Pennsylvania State University, Cleveland, OH, October 26-27, 2000.

[2] Santoro, R. J., Pal, S., Woodward, R. D. and Schaaf, L., "Rocket Testing at University Facilities," AIAA-2001-0748, 39th AIAA Aerospace Sciences Meeting and Exhibit, Reno, NV, January 8-11, 2001.

[3] Cramer, J. M., Greene, M., Pal, S. and Santoro, R. J., "RBCC Ejector Mode Operating Characteristics for Single and Twin Thruster Configurations," AIAA-2001-3464, 37th AIAA/ASME/SAE/ASEE Joint Propulsion Conference, Salt Lake City, UT, July 8-11, 2001.

[4] Ruf, J., Lehman, M., Pal, S., Santoro, R. J. and West, J., "Experimental/Analytical Characterization of the RBCC Rocket-Ejector Mode," 37th JANNAF Combustion Subcommittee Meeting, Monterey, CA, November 13-17, 2000.

[5] Cramer, J. M., Greene, M. U., Pal, S. and Santoro, R. J., "Characterization of Mixing and Combustion Processes in a Rocket-Based Combined Cycle (RBCC) Flow Field Using Raman Spectroscopy," Technical Meeting of the Eastern States Section of The Combustion Institute, Hilton Head, SC, December 3-5, 2001.

[6] Cramer, J. M., Greene, M. U., Pal, S., and Santoro, R. J., "Sea-Level Static Performance of a Rocket-based Combined Cycle Test Article," Propulsion Engineering Research Center, Penn State, Thirteenth Annual Symposium, The Pennsylvania State University, Huntsville, AL, October 22-23, 2001.

[7] Greene, M. U., Cramer, J. M., Pal, S., and Santoro, R. J., "Experimental Study of the RBCC Rocket-Ejector Mode for JP-7/GO_2 Propellants," Propulsion Engineering Research Center, Penn State, Thirteenth Annual Symposium, The Pennsylvania State University, Huntsville, AL, October 22-23, 2001.

10. PERSONNEL

Robert J. Santoro, George L. Guillet Professor of Mechanical and Nuclear Engineering, co-Principal Investigator

Sibtosh Pal, Senior Research Associate, Department of Mechanical and Nuclear Engineering co-Principal Investigator

John Cramer, Ph.D Student, Department of Mechanical and Nuclear Engineering

Mayumi U. Greene, MS 2002, Department of Mechanical and Nuclear Engineering

Matthew Lehman, Ph.D. 2000, Department of Mechanical and Nuclear Engineering

Larry Schaaf, Senior Research Technician, Department of and Nuclear Mechanical Engineering